Boreal Summer Synoptic-Scale Waves over the Western North Pacific in Multimodel Simulations

HAIKUN ZHAO

Key Laboratory of Meteorological Disaster, Ministry of Education (KLME), and Joint International Research Laboratory of Climate and Environment Change (ILCEC), and Collaborative Innovation Center on Forecast and Evaluation of Meteorological Disasters, and Pacific Typhoon Research Center, and Earth System Modeling Center, Nanjing University of Information Science and Technology, Nanjing, China, and Joint Institute for Regional Earth System Science and Engineering, University of California, Los Angeles, Los Angeles, California

XIANAN JIANG

Joint Institute for Regional Earth System Science and Engineering, University of California, Los Angeles, Los Angeles, and Jet Propulsion Laboratory, California Institute of Technology, Pasadena, California

LIGUANG WU

Pacific Typhoon Research Center, Key Laboratory of Meteorological Disaster of Ministry of Education, Nanjing University of Information Science and Technology, Nanjing, China

(Manuscript received 2 October 2015, in final form 8 March 2016)

ABSTRACT

During boreal summer, vigorous synoptic-scale wave (SSW) activity, often evident as southeast–northwest-oriented wave trains, prevails over the western North Pacific (WNP). In spite of their active role for regional weather and climate, modeling studies on SSWs are rather limited. In this study, a comprehensive survey on climate model capability in representing the WNP SSWs is conducted by analyzing simulations from 27 recent general circulation models (GCMs). Results suggest that it is challenging for GCMs to realistically represent the observed SSWs. Only 2 models out of the 27 GCMs generally well simulate both the intensity and spatial pattern of the observed SSW mode. Plausible key processes for realistic simulations of SSW activity are further explored. It is illustrated that GCM skill in representing the spatial pattern of the SSW is highly correlated to its skill in simulating the summer mean patterns of the low-level convergence associated with the WNP monsoon trough and conversion from eddy available potential energy (EAPE) to eddy kinetic energy (EKE). Meanwhile, simulated SSW intensity is found to be significantly correlated to the amplitude of 850-hPa vorticity, divergence, and conversion from EAPE to EKE over the WNP. The observed modulations of SSW activity by the Madden–Julian oscillation are able to be captured in several model simulations.

1. Introduction

During boreal summer, one of the most prominent weather phenomena over the western North Pacific (WNP) is the frequent occurrence of synoptic-scale waves (SSWs), often evident as wave trains aligned in a southeast–northwest direction with a typical wavelength of about 2500–3000 km and a time scale of 3–8 days (Wallace and Chang 1969; Chang et al. 1970; Reed and Recker 1971; Lau and Lau 1990; Sobel and Bretherton 1999; Maloney and Dickinson 2003; Tam and Li 2006; Li 2006; and many others). These SSWs not only exert significant impacts on extreme rain events in the Asian monsoon region (e.g., Chen and Weng 1996; Chen et al. 2011; Wu et al. 2011; Fukutomi et al. 2015), they also serve as critical "seeding" for geneses of a majority of tropical cyclones (TCs) over the WNP (Wallace 1971; Zehr 1992; Holland 1995; Ritchie and Holland 1997; Li and Fu 2006; Takayabu and Nitta 1993; Chen and Huang 2009; Chen and Chou 2014; Serra et al. 2014). The SSWs could also play an important role in sustaining larger-scale systems—for example, by contributing to the amplification and northward propagation of the boreal summer Madden–Julian oscillation (MJO) over the

Corresponding author address: Dr. Xianan Jiang, Jet Propulsion Laboratory, California Institute of Technology, MS 233-300, 4800 Oak Grove Drive, Pasadena, CA 91109.
E-mail: xianan@ucla.edu

DOI: 10.1175/JCLI-D-15-0696.1

WNP through upscale transport of moisture, heat, momentum, and surface fluxes (Zhou and Li 2010; Hsu and Li 2011; Hsu et al. 2011; Li 2014). In this study, the term SSW is used to specifically represent the southeast–northwest-oriented synoptic wave train over the WNP. These synoptic waves have also been referred to as easterly waves, tropical depression–type disturbances, or synoptic-scale disturbances in many other studies (e.g., Riehl 1945; Takayabu and Nitta 1993; Dunkerton and Baldwin 1995; Sobel and Bretherton 1999).

It has been suggested that the preference of the SSWs over the WNP during boreal summer is closely associated with the unique Asian summer monsoon circulation (Lau and Lau 1990; Sobel and Bretherton 1999; Ritchie and Holland 1999; Li 2006; Straub and Kiladis 2003; Maloney and Dickinson 2003; Kuo et al. 2001; Holland 1995; Yoshida and Ishikawa 2013). The low-level summer mean circulation over the WNP is featured by a monsoon trough, a strong zonal confluence zone due to cross-equatorial southwesterlies from the west and easterly low-level winds from the east. Two primary energy sources, barotropic conversion and eddy available potential energy (EAPE), have been identified to play critical roles in sustaining eddy kinetic energy (EKE) associated with SSWs over the WNP (Lau and Lau 1992; Maloney and Hartmann 2001; Maloney and Dickinson 2003; Wu et al. 2014). While the former is mainly through conversion of EKE from the mean kinetic energy (MKE) by both convergent and rotational components of mean zonal flow, the latter is largely produced by vigorous latent heat release from cumulus convection. Particularly, the importance of wave accumulation in shaping the SSW activity over the WNP associated with barotropic conversion by convergent mean flow has been emphasized in many previous studies (Tai and Ogura 1987; Holland 1995; Sobel and Bretherton 1999; Sobel and Maloney 2000; Kuo et al. 2001; Maloney and Dickinson 2003; Tam and Li 2006; Wu et al. 2014).

An idealized model study also suggested that an easterly vertical shear of the monsoonal circulation over the WNP could be crucial for the observed SSWs in the presence of a convection–frictional convergence feedback (Li 2006). Other processes were also proposed to be important for SSW development, including Rossby wave energy dispersion from a preexisting TC (Holland 1995; Ritchie and Holland 1999; Li et al. 2003; Li and Fu 2006; Li et al. 2006) and the transition of equatorial mixed Rossby–gravity (MRG) waves when propagating into the WNP (Liebmann and Hendon 1990; Dunkerton 1993; Takayabu and Nitta 1993; Dunkerton and Baldwin 1995; Dickinson and Molinari 2002; Aiyyer and Molinari 2003; Tam and Li 2006; Zhou and Wang 2007; Chen and Huang 2009).

In agreement with significant roles of the aforementioned processes associated with the environmental circulation in energizing SSWs, modulation of SSW activity by large-scale climate variability modes has been widely reported, including by El Niño–Southern Oscillation (ENSO) (e.g., Sobel and Maloney 2000; Chen and Huang 2009; Chen 2012; Wu et al. 2014), the Pacific–Japan teleconnection pattern (Li et al. 2014), and the MJO (e.g., Sobel and Maloney 2000; Maloney and Hartmann 2001; Maloney and Dickinson 2003; Zhou and Li 2010; Hsu et al. 2011). For example, as the dominant tropical intraseasonal variability (ISV) mode, the MJO can significantly modulate the summer mean background circulation over the WNP. When the convection associated with the northwestward-propagating boreal summer MJO becomes active over the WNP, the mean monsoon trough is intensified, thus favoring enhancement of the local SSW activity (Sobel and Maloney 2000; Maloney and Hartmann 2001; Maloney and Dickinson 2003; Zhou and Li 2010; Hsu and Li 2011) and associated TC activity (e.g., Liebmann et al. 1994; Wang and Zhou 2008; Nakazawa 1988; Zhao et al. 2015). Detailed characterization of factors associated with the MJO modulation on SSW activity over the WNP could provide valuable insights into key processes regulating SSW activity.

In light of the significance of SSWs for regional weather and climate, accurate prediction of SSW activity could greatly help improve weather as well as extended-range forecasts (e.g., Xiang et al. 2015). While there have been some modeling studies in exploring how synoptic-scale tropical waves are represented in general circulation models (GCMs), most of them have focused on the convectively coupled equatorial waves (CCEWs) (e.g., Suzuki et al. 2006; Lin et al. 2006, 2008; Straub et al. 2010; Frierson et al. 2011; Seo et al. 2012; Hung et al. 2013; Huang et al. 2013). Model studies on the assessment of GCM fidelity in representing SSWs over the WNP are particularly limited. Tulich et al. (2011) examined convectively coupled Kelvin waves and SSWs in simulations of the global tropics using the tropical channel Weather Research and Forecasting (WRF) Model. The model SSW activity is generally too active over the Indian Ocean and WNP compared to the observations, which could possibly be responsible for too-frequent TC genesis in these regions in model simulations.

Huang et al. (2013) also briefly examined variances of SSWs and several CCEWs simulated by 10 coupled GCMs participating in phase 3 of the Coupled Model

Intercomparison Project (CMIP3) of the World Climate Research Programme. Their results suggest that the observed northwestward propagation of SSWs over the WNP was not well simulated in most GCMs. The active SSW activity is evident only from June to August in model simulations, rather than from June to October as in the observations. A similar model deficiency in simulating the seasonal cycle of SSW activity over the WNP was also noted by a recent study based on a global cloud-system-resolving model (CRM) with a 14-km horizontal resolution (Fukutomi et al. 2016). While the CRM is able to well capture the observed horizontal and vertical structure of SSWs as well as their northwestward propagation, the latitude of the maximum SSW activity tends to be displaced to the north of its observed counterpart by a few degrees. This northward displacement of SSW activity in CRM simulations was further attributed to model biases in simulating the structure and strength of the background mean flow (Fukutomi et al. 2016).

In this study, model capability in representing the SSW over the WNP in the latest generation of GCMs is examined by analyzing multimodel simulations from a recent global model evaluation project coordinated by the MJO Task Force (MJOTF), under the auspices of the Year of Tropical Convection (YOTC; Moncrieff et al. 2012; Waliser et al. 2012)[1] and the Global Energy and Water Exchanges project (GEWEX) Atmospheric System Study (GASS) (hereafter the MJOTF/GASS MJO project; Petch et al. 2011; Jiang et al. 2015). While the main focus of the MJOTF/GASS MJO project is to explore key physical processes for the MJO, the long-term 3D output with high temporal resolution from 27 model simulations provides an excellent opportunity to examine model fidelity in representing the SSWs and to identify key processes responsible for realistic SSW simulations in climate models. The organization of this manuscript is as follows. The MJOTF/GASS MJO project and observational datasets used for this study are described in section 2. In section 3, model fidelity in representing the summer mean state and general SSW activity over the WNP in 27 MJOTF/GASS climate simulations is presented. The approach in identifying the leading SSW mode over the WNP based on observations and models is introduced, and model fidelity in depicting the leading SSW mode is illustrated in section 4. Key processes responsible for high-quality simulations of model SSW activity are further explored in section 5. Modulation of SSW activity by the boreal summer MJO over the WNP in both observations and selected model simulations will be further illustrated in section 6. Finally, a summary is given in section 7.

2. Data and methodology

a. *Multimodel dataset from the MJOTF/GASS MJO project*

The MJOTF/GASS MJO project consists of three experimental components, including a 20-yr climate simulation (Jiang et al. 2015), a 2-day hindcast (Xavier et al. 2015), and a 20-day hindcast component (Klingaman et al. 2015). In this study, we mainly analyze multimodel simulations from the 20-yr climate simulation component of this project, which includes 27 simulations from 24 GCMs. A list of these participating models along with their horizontal and vertical resolutions is shown in Table 1. All participating models in the climate simulation component, with either an atmosphere-only GCM (AGCM) or an atmosphere–ocean coupled system, were integrated for 20 years. For AGCM runs, weekly sea surface temperature (SST) and sea ice concentrations based on the National Oceanic and Atmospheric Administration (NOAA) Optimum Interpolation SST version 2 product (Reynolds et al. 2002) for the 20-yr period of 1991–2010 were specified as the model lower boundary conditions. Output from all participating GCMs was archived at every 6 h on standard horizontal (2.5° × 2.5°) grids and 22 vertical pressure levels. Details on the MJOTF/GASS global MJO project, particularly its climate simulation component, can be found in Jiang et al. (2015), in which model skill in representing the MJO was reported along with efforts to discriminate key processes responsible for realistic simulation of the MJO in these models.

While a conventional parameterization approach in depicting cumulus processes is used in most of these models, two experiments, SPCCSM3 and SPCAM3, adopted the ''superparameterization'' technique based on the National Center for Atmospheric Research (NCAR) Community Atmosphere Model (CAM) to replace the model cumulus parameterization module (Randall et al. 2003). The SPCAM3 is an atmosphere-only version (Khairoutdinov et al. 2008), and the SPCCSM3 is a coupled atmosphere–ocean run based on the same AGCM (Stan et al. 2010). Previous studies reported that greatly improved simulations of the mean state as well as climate variability can be achieved in these superparameterized GCMs

[1] Note that the MJOTF was recently reformulated and now is under the auspices of the Working Group on Numerical Experimentation (WGNE).

TABLE 1. GCMs analyzed in this study with horizontal resolutions (lon × lat with spectral model resolution in parentheses) and vertical levels. Atmosphere–ocean coupled simulations are denoted by asterisks by the model names. (Expansion of acronyms are available online at http://www.ametsoc.org/PubsAcronymList.)

	Model name	Institute and country	Horizontal resolution, vertical levels
1	ACCESS1.0	Centre for Australian Weather and Climate Research, Australia	1.875° × 1.25°, L85
2	BCC_AGCM2.1	Beijing Climate Center, China Meteorological Administration, China	2.8° (T42), L26
3	CAM5	National Center for Atmospheric Research, United States	1.25° × 0.9°, L30
4	CAM5-ZM	Lawrence Livermore National Laboratory, United States	1.25° × 0.9°, L30
5	CanCM4*	Canadian Centre for Climate Modelling and Analysis, Canada	2.8°, L35
6	CFSv2	Climate Prediction Center, NOAA/NCEP, United States	1° (T126), L64
7a	CNRM-AM	Centre National de Recherches Météorologiques (CNRM)/Météo-France, France	1.4° (T127), L31
7b	CNRM-CM*		
7c	CNRM-ACM		
8	CWB Global Forecast System (CWB-GFS)	Central Weather Bureau (CWB), Taiwan	1° (T119), L40
9	EC-EARTH3	Rossby Centre, Swedish Meteorological and Hydrological Institute, Sweden	80 km (T255), L91
10	EC-GEM	Environment Canada, Canada	1.4°, L64
11	ECHAM5-SIT*	Academia Sinica, Taiwan	2° (T63), L31
12	ECHAM6*	Max Planck Institute for Meteorology, Germany	2° (T63), L47
13	FGOALS-s2	Institute of Atmospheric Physics, Chinese Academy of Sciences, China	2.8° × 1.6° (R42), L26
14	GEOS-5	NASA Global Modeling and Assimilation Office, United States	0.625° × 0.5°, L72
15	GISS-E2	NASA Goddard Institute for Space Studies, United States	2.5° × 2.0°, L40
16	ISUGCM	Iowa State University, United States	2.8° (T42), L18
17	Met Office Unified Model–Global Atmosphere, version 3 (MetUM-GA3)	Met Office, United Kingdom	1.875° × 1.25°, L85
18	MIROC5	Atmosphere and Ocean Research Institute (AORI)/National Institute for Environmental Studies (NIES)/JAMSTEC, Japan	1.5° (T85), L40
19	MRI-AGCM3	Meteorological Research Institute, Japan	1.125° (T159), L48
20	NavGEM1	Naval Research Laboratory, United States	37 km (T359), L42
21	PNU-CFS*	Pusan National University, South Korea	2° (T62), L64
22a	SPCAM3	Colorado State University, United States	2.8° (T42), L30
22b	SPCCSM3*	George Mason University, United States	2.8° (T42), L30
23	TAMU-CAM4	Texas A&M University, United States	2.5° × 1.9°, L26
24	UCSD-CAM3	Scripps Institution of Oceanography, United States	2.8° (T42), L26

(Benedict and Randall 2007; Stan et al. 2010; DeMott et al. 2012; Pritchard and Bretherton 2014). It would be interesting to examine how SSWs over the WNP are represented in these two superparameterized simulations.

Also noteworthy is that three integrations were conducted based on the CNRM GCMs, including an AGCM integration forced by the observed weekly SST and sea ice (CNRM-AM), a CGCM run (CNRM-CM), and a third experiment in which the AGCM was forced by the monthly mean SST and sea ice output from the coupled run (CNRM-ACM). While the atmosphere–ocean interaction was found to play a crucial role for realistic simulations of the MJO in this model (Jiang

et al. 2015), it is also intriguing to examine how air–sea interaction might influence model simulations of the SSW.

b. Observational datasets

Rainfall observations based on the Tropical Rainfall Measuring Mission [TRMM 3B42 product, version 7 (V7); Huffman et al. 1995] during the period of 1998–2012 are used to identify the leading SSW and MJO modes over the WNP. TRMM 3B42 rainfall is a global precipitation product based on multisatellite and rain gauge analyses. It provides precipitation estimates with 3-hourly temporal resolution on a 0.25° spatial resolution in a global belt extending from 50°S to 50°N.

The European Centre for Medium-Range Weather Forecasts (ECMWF) interim reanalysis (ERA-Interim; Dee et al. 2011) with a horizontal grid resolution of 1.5° × 1.5° is also used in this study. It provides daily 3D profiles of temperature, specific and relative humidity, winds, and pressure vertical velocity. To be consistent with the output in climate models, both the raw TRMM rainfall and ERA-Interim data are interpolated onto 2.5° × 2.5° and 22 standard vertical pressure levels. Analyses presented in this study are mainly based on daily averaged values if not particularly mentioned.

3. Summer mean state and SSW activity in multimodel simulations

a. Summer mean state

In this part, model fidelity in representing the summer mean state over the WNP is first examined. Figure 1 displays summer mean (May–October) rainfall and 850-hPa winds for the observations and 27 GCM simulations. The observed summer mean rainfall over the WNP (Fig. 1, top left) is characterized by a southeast–northwest-tilted rainband collocated with a low-level convergent zone between monsoon westerlies and easterlies associated with the Pacific subtropical high, known as the WNP monsoon trough. Regional rainfall maxima are also evident to the west of Vietnam and over the South China Sea to the west of the Philippines, representing orographic impacts on the Asian monsoon (e.g., Xie et al. 2006).

A majority of the GCMs have difficulties in capturing the observed southeast–northwest-slanted summer mean rain belt and low-level circulation associated with the WNP monsoon trough. Substantially weaker monsoon circulations and rainfall than the observations over the WNP are noted in several GCMs, including CAM5, CAM5 with Zhang–McFarlane convective parameterization (CAM5-ZM), CFSv2, CNRM-ACM, Iowa State University GCM (ISUGCM), MIROC5, and Texas A&M University CAM version 4 (TAMU-CAM4). In contrast, stronger low-level monsoonal flow and mean rainfall than the observations are simulated in several other GCMs, including ACCESS1.0, BCC AGCM version 2.1 (BCC_AGCM2.1), EC-EARTH version 3 (EC-EARTH3), Environment Canada Global Environment Model (EC-GEM), ECHAM5 with snow–ice–thermocline coupler (ECHAM5-SIT), GISS-E2, MRI-AGCM3, SPCAM3, and University of California, San Diego, CAM version 3 (UCSD-CAM3). While most of these GCMs exhibit large deficiencies in depicting the intensity of the summer monsoon over the WNP, several GCMs are able to reasonably capture spatial patterns in both summer mean rainfall and 850-hPa winds (e.g., CAM5, CNRM-CM, CNRM-ACM, EC-EARTH3, MRI-AGCM3, and SPCCSM3). Noteworthy is the significant improvement in the summer mean state in simulations from CNRM-CM and CNRM-ACM compared to the CNRM-AM run. Considering that monthly mean SST used in CNRM-ACM was generated from the coupled simulations of CNRM-CM, the great similarity in summer mean patterns in CNRM-CM and CNRM-ACM suggests that improvement achieved in the CNRM-CM and CNRM-ACM over the CNRM-AM is mainly due to differences between simulated SSTs in CNRM-CM and the observed SSTs specified in CNRM-AM. It is also noticed that the atmosphere-only superparameterized experiment (i.e., SPCAM3) also exhibits large biases in depicting the WNP monsoon trough, while a significant improvement is noted in the coupled version of this model (SPCCSM3).

b. The 3–8-day synoptic-scale variability

Figure 2 further examines the spatial distribution of the amplitude of general synoptic-scale variability (SSV) in both observations and model simulations by showing the standard deviation (STD) of 3–8-day bandpass-filtered rainfall anomalies during boreal summer (May–October). The STD pattern of the observed SSV largely follows its summer mean rainfall pattern, with the strongest SSV evident along the southeast–northwest convergence zone of the WNP monsoon trough and a maximum activity center near 15°N, 120°E. The SSV amplitude is significantly underestimated in a majority of GCM simulations while overestimated in several other GCMs, including BCC_AGCM2.1, GISS-E2, MRI-AGCM3, and UCSD-CAM3. Stronger SSV amplitudes largely follow

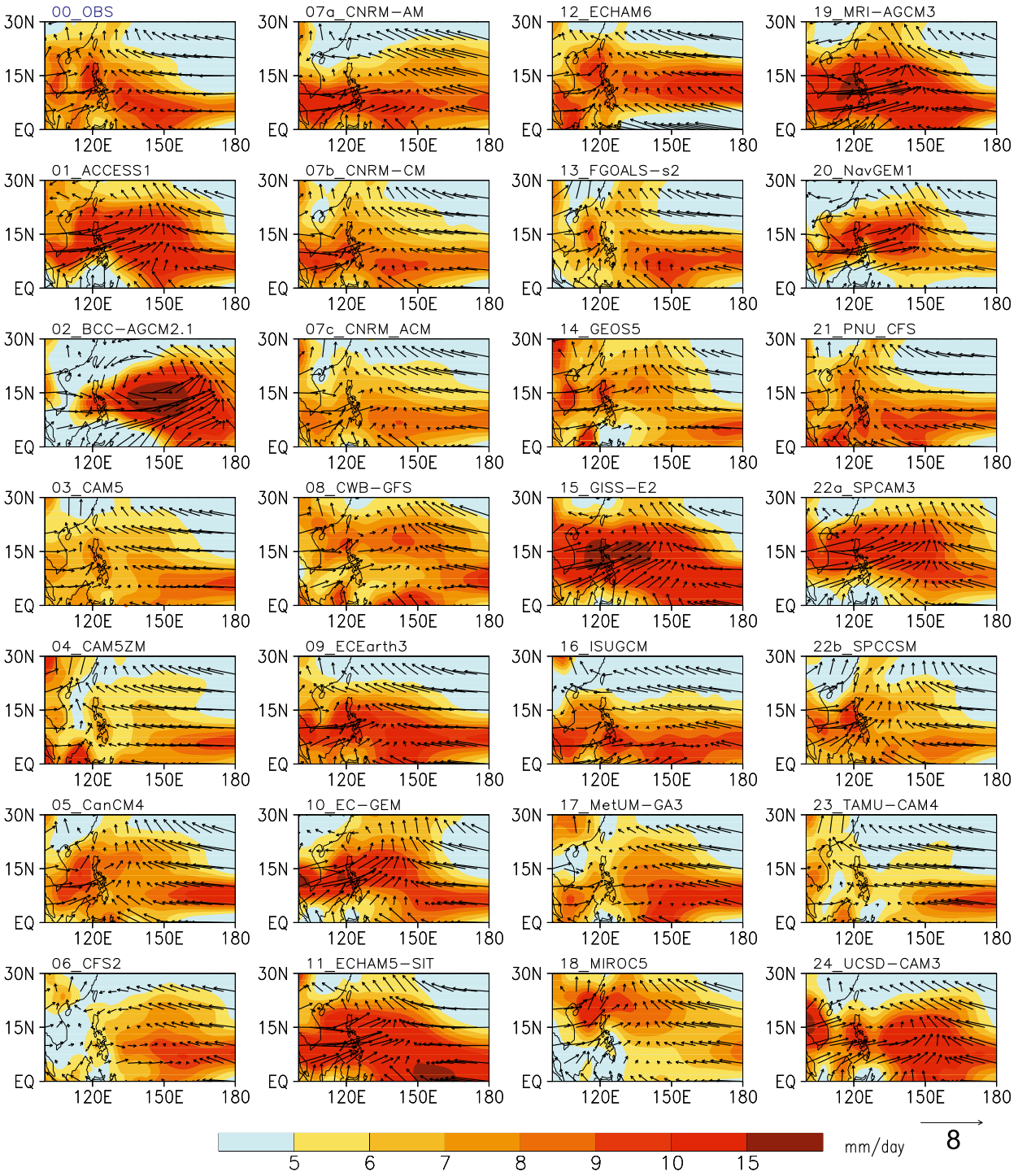

FIG. 1. Observed and simulated summer mean (May–October) rainfall patterns (mm day^{-1}; shaded, see color bar at the bottom) and 850-hPa winds (m s^{-1}; vectors). Observed rainfall and winds are based on TRMM and ERA-Interim, respectively, for the period 1998–2012, while model mean state is based on 20-yr simulations.

stronger summer mean rainfall over the WNP across these model simulations, although exceptions are also noted. For example, while stronger than the observed summer mean rainfall is simulated in ACCESS1.0, ECHAM5-SIT, and SPCAM3, the SSV amplitudes in these model simulations are rather weak. Also note that both the superparameterized GCM simulations show large biases in representing spatial distribution

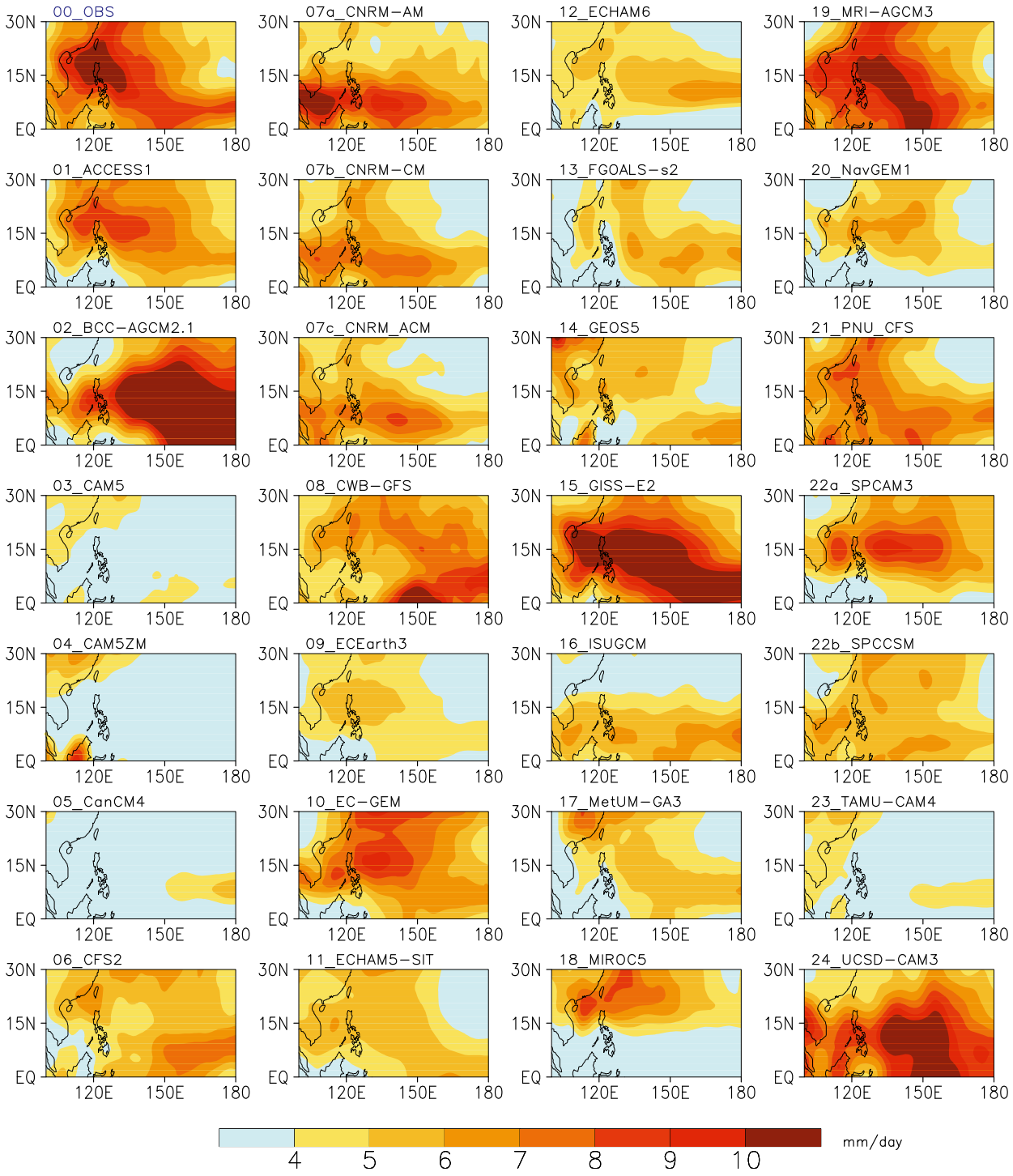

FIG. 2. Standard deviations of 3–8-day bandpass-filtered rainfall anomalies (mm day^{-1}) during boreal summer (May–October).

of SSV activity, indicating that other model physics in addition to cumulus processes could also be critical for realistic simulations of the SSV over the WNP. Similar to model skill for the summer mean rainfall pattern, model capability in capturing the general SSV activity over the WNP varies widely across climate models.

In the next section, we further evaluate how the spatial pattern of the observed SSW mode over the WNP is represented in climate models.

4. Simulation of the SSW over the WNP in climate models

a. *Identification of the leading SSW mode over the WNP*

To identify the leading SSW mode over the WNP in both observations and model simulations, an extended empirical orthogonal function (EEOF) analysis method (Weare and Nasstrom 1982) is applied to 3–8-day bandpass-filtered daily rainfall anomalies over the WNP region of 0°–30°N, 100°–160°E, for the boreal summer season (May–October). Prior to 3–8-day temporal filtering, daily rainfall anomalies based on both TRMM and model simulations were obtained by removing annual mean and three leading annual harmonics. The southeast–northwest-slanted wave train of the observed SSW mode, as widely reported in previous studies (e.g., Lau and Lau 1990; Takayabu and Nitta 1993; Sobel and Bretherton 1999; Li 2006; Chen and Huang 2009), is readily seen by the leading pair of EEOF modes based on TRMM rainfall (refer to Fig. 3a, although derived by regressions based on reconstructed rainfall anomalies from the observed EEOF1 and EEOF2 as mentioned below). The two leading EEOF modes are in quadrature with each other, representing propagation features of the observed SSWs.

Daily rainfall anomalies associated with the dominant SSW mode over the WNP for both observations and model simulations can then be derived by the first two leading EEOF modes and corresponding principal components (PCs)—namely, PC1 × EEOF1 + PC2 × EEOF2. In the following, we refer to these reconstructed rainfall anomalies for the leading SSW mode as PR_{rec} and 3–8-day bandpass-filtered rainfall anomalies as $PR_{3–8d}$. Meanwhile, SSW amplitudes can be denoted by the STD of daily PR_{rec}. Spatial evolution of rainfall anomalies associated with the dominant SSW mode can be further derived by lead–lag regressions of PR_{rec} against its averaged value over a 5° × 5° box centered at the location 15°N, 130°E, for both observations and simulations. Other variables associated with the SSW can also be similarly obtained by regressing 3–8-day bandpass-filtered fields of these variables onto the same time series of area-averaged PR_{rec} anomalies.

Figure 3a shows the lag-0 rainfall regression pattern (shaded) of the observed dominant SSW mode by utilizing the EEOF-based reconstructed TRMM rainfall anomalies. Corresponding 850-hPa winds (vectors) based on ERA-Interim are also displayed by simultaneously regressing 3–8-day-filtered wind anomalies onto the same box-averaged PR_{rec} anomalies. Readily seen in Fig. 3a is a well-defined southeast–northwest-tilted wave train with enhanced (reduced) rainfall anomalies collocated with cyclonic (anticyclonic) low-level circulations, in agreement with many previous studies (e.g., Lau and Lau 1990; Takayabu and Nitta 1993; Chen and Huang 2009).

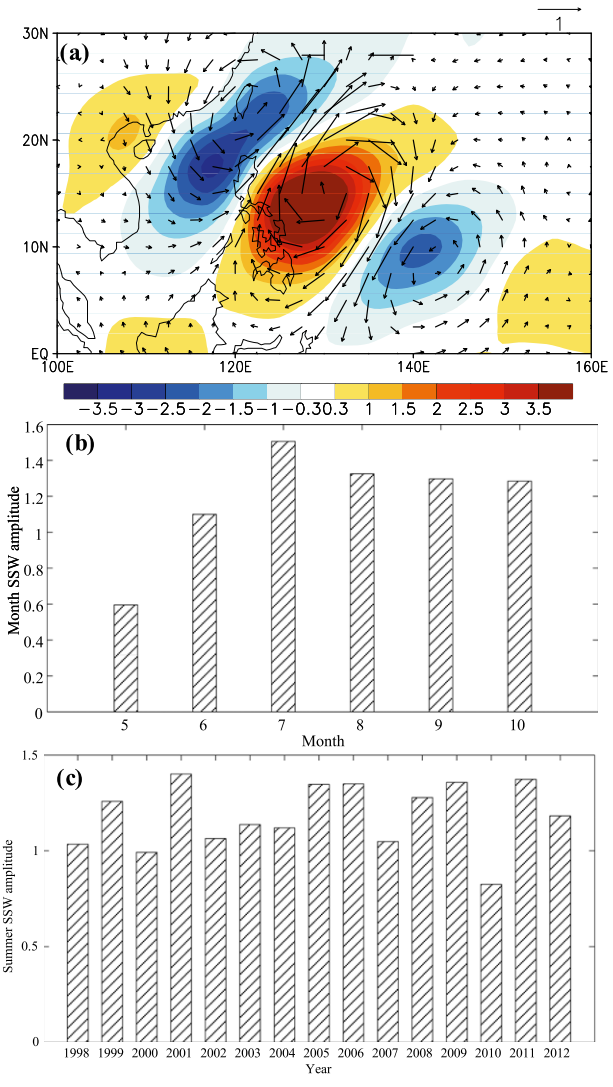

FIG. 3. (a) Lag-0 regression patterns of 850-hPa winds ($m\,s^{-1}$; vectors with a scale at top right) and rainfall ($mm\,day^{-1}$; shaded) associated with the observed SSW mode over the WNP. Regressions were calculated against reconstructed rainfall anomalies over a 5° × 5° box near 15°N, 130°E. See text for details. (b) Climatologically seasonal evolution (May–October) and (c) interannual variability of SSW amplitude.

The climatological seasonal evolution of SSW activity over the WNP in observations as defined by the two PCs of the leading EEOF modes ($\sqrt{PC_1^2 + PC_2^2}$) based on TRMM rainfall for the period of 1998–2012 is illustrated in Fig. 3b. It is clearly seen that the amplitude of SSWs significantly increases in June, reaches a maximum in July, and then remains at a high activity level until

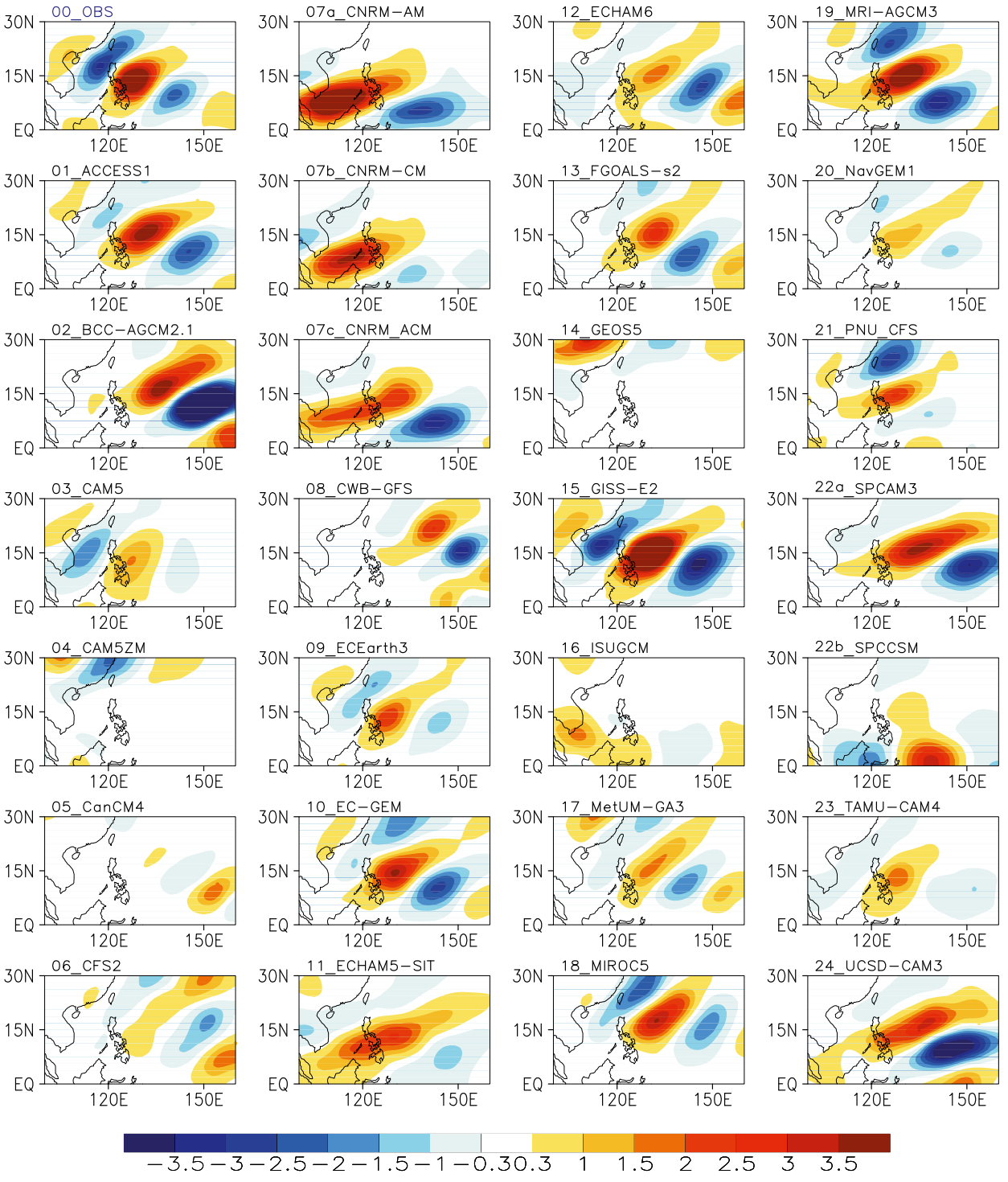

FIG. 4. As in Fig. 3a, but for lag-0 regressed rainfall patterns (mm day^{-1}) in 27 GCM simulations. (top left) The observed SSW pattern is also displayed for comparison.

October. Moreover, pronounced interannual variations in summertime SSW activity during the period of 1998–2012 are clearly illustrated in Fig. 3c. Particularly noteworthy is the weakest SSW amplitude during the summer of 2010, corresponding to the quietest TC activity over the WNP in 2010 during this period (Liu and Chan 2013; Kim et al. 2012; Zhao et al. 2014; Zhao and Raga 2014). Whether reduced SSW and TC activity

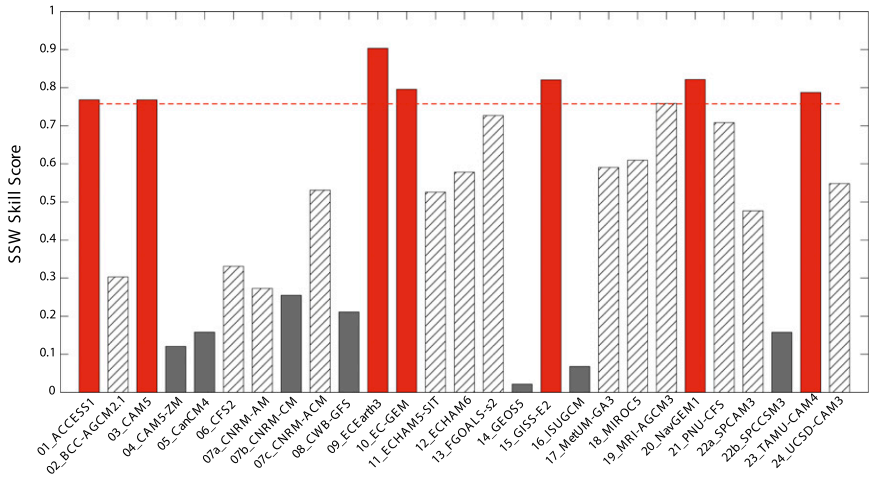

FIG. 5. Model skill scores in simulating SSW patterns over the WNP derived by pattern correlations of simulated leading SSW patterns against the observations. See text for details to derive the leading SSW modes in observations and model simulations. Red (dark gray) bars denote roughly the top (bottom) 25% GCMs in simulating the WNP SSW pattern.

during 2010 were affected by the same large-scale factors, or the damped TC activity was due to a reduced seeding effect from the SSW, warrants further investigation.

b. *GCM fidelity in representing the dominant SSW mode over the WNP*

Similar to Fig. 3a for the observations, spatial patterns of rainfall anomalies associated with the leading SSW mode simulated in 27 climate simulations are shown in Fig. 4 along with the observations. Interestingly, the southeast–northwest alignment of the wave train over the WNP associated with the leading SSW mode can be discerned in many GCMs, although simulated SSW modes exhibit a variety of deficiencies compared to the observations, including the amplitude, location of the maximum activity center, spatial scale of wave patterns, and tilting direction of the wave train axis, and so forth. Based on the lag-0 rainfall patterns, two GCMs (i.e., ACCESS1.0 and GISS-E2) exhibit the most realistic simulations of the observed dominant SSW mode over the WNP in both amplitude and spatial pattern.

To objectively quantify model capability of simulating the SSW mode, pattern correlations are calculated based on the evolution of 2D rainfall patterns of simulated leading SSW mode over the WNP domain (0°–30°N, 100°–160°E) from lag −2 to lag 2 days with an interval of one day against their observational counterpart. As previously described, the 2D evolution patterns of observed or simulated SSW modes are obtained by the lag regression of PR_{rec} rainfall against a base point (15°N, 130°E). Note that the model skill in representing both the spatial distribution and time scale of the leading SSW mode is taken into account by pattern correlations based on a sequential evolution of 2D SSW patterns. The pattern correlation skill score for the SSW mode in each model is shown in Fig. 5. Seven models (denoted by red bars) exhibit relatively high skill in capturing the observed SSW pattern with pattern correlation scores greater than 0.76, including ACCESS1.0, CAM5, EC-EARTH3, EC-GEM, GISS-E2, Naval Research Laboratory Global Environment Model version 1 (NavGEM1), and TAMU-CAM4. In the following, we define these seven GCMs as good SSW models, roughly representing the top 25% models among the 27 GCMs evaluated. Similarly, seven GCMs with the lowest pattern correlation scores (dark bars in Fig. 5) are selected as bad SSW models for an attempt to discriminate key processes for realistic simulations of the WNP SSW. However, it is worth noting that determination of these good and bad GCMs is only based on the spatial patterns of the simulated leading SSW mode; some good GCMs actually also exhibit significant biases in simulating the SSW amplitude.

It is noteworthy that while adoption of the superparameterization approach can lead to significant improvement in simulations of various aspects of tropical mean climate and variability (e.g., Benedict and Randall 2007; Stan et al. 2010; Jiang et al. 2012; DeMott et al. 2014; Jiang et al. 2015), results in this study illustrate that superparameterized GCMs also have great difficulty in simulating the regional mean monsoon and the observed SSW mode over the WNP during the boreal summer. This suggests that other model physics in addition to cumulus processes could also be critical for realistic simulations of regional climate over the WNP. On the other

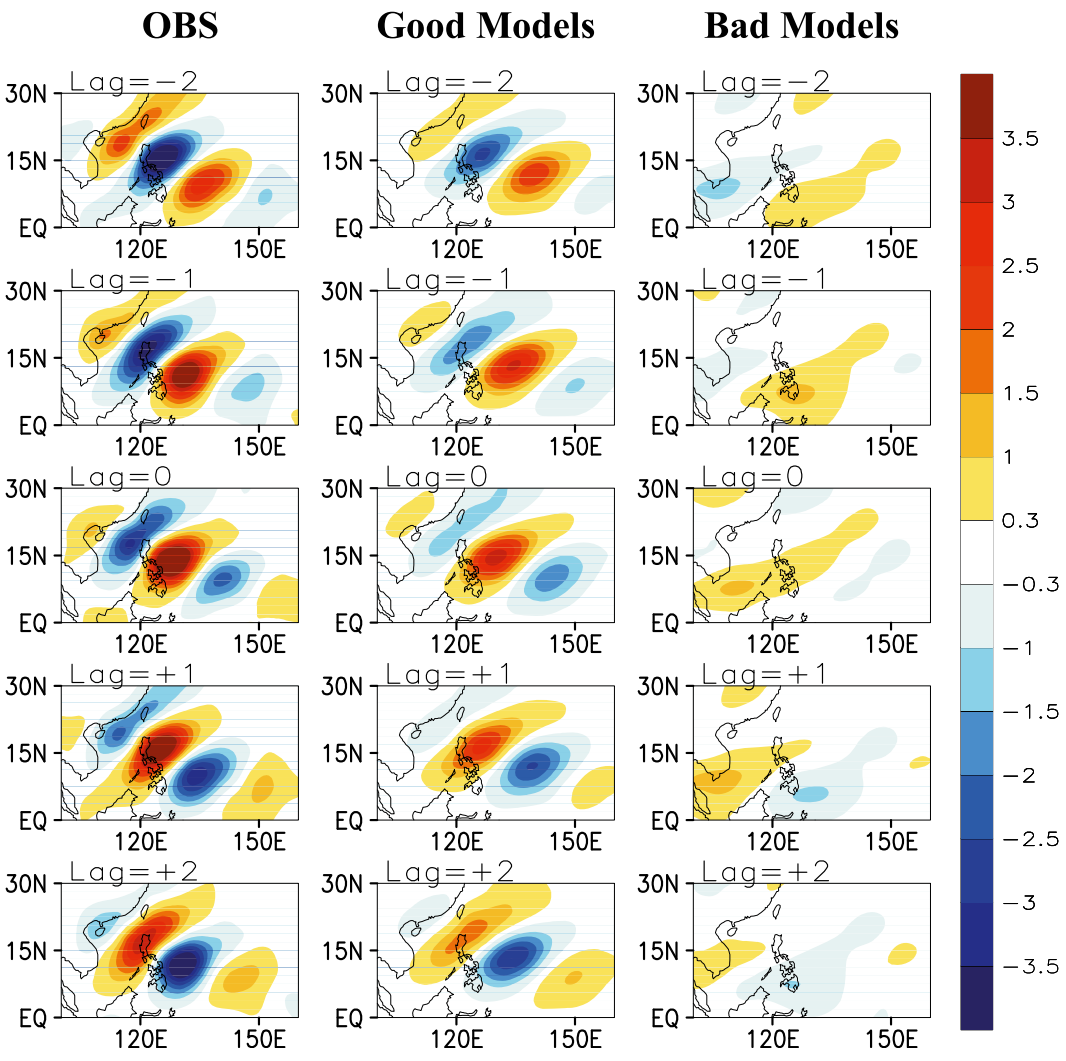

FIG. 6. Evolution of SSW patterns (mm day^{-1}) from lag −2 to lag 2 days for (left) the observations and composite based on seven (center) good and (right) bad models.

hand, realistic representation of the SSW mode in atmosphere-only GCMs (e.g., ACCESS1.0 and GISS-E2) suggests that internal atmospheric processes play a critical role for the SSW mode over the WNP.

The evolution of rainfall patterns associated with the SSW mode in the observations and the composite based on seven good and bad models are further illustrated in Fig. 6. Clearly evident is that the well-defined southeast–northwest alignment of the wave train associated with the observed SSW is well represented in good model composites, including both the pattern and amplitude. In contrast, the leading SSW mode in bad model composites is rather weak and displays an alignment in an east–west direction.

In the following analyses, pattern correlation scores for the leading SSW modes across these 27 GCMs will be used as a primary index of model skill in simulating the SSW pattern to explore critical large-scale factors responsible for realistic SSW simulations. In addition to the spatial pattern, factors regulating the SSW amplitude across model simulations will also be examined.

5. Key factors responsible for SSW simulations in GCMs

a. Spatial pattern of the leading SSW mode over the WNP

As previously mentioned, the observed SSW over the WNP is intimately due to instability processes associated with the summer mean state. In this part, in order to identify key large-scale factors for high-quality model

TABLE 2. Correlations between SSW pattern skill scores and model skill in simulating large-scale summer mean patterns across multimodel simulations. Significant correlations at a 99% confidence level are indicated by asterisks.

Model variable	Correlation
Summer rainfall	0.25
u850	0.34
u shear (u850 − u200)	0.25
850-hPa relative vorticity	0.23
850-hPa divergence	0.60*
Vertically averaged EKE	0.54*
Vertically averaged $\overline{w'T'}$	0.67*

simulations of the SSW pattern, correlations are calculated between model skill in simulating summer mean patterns, including rainfall, 850-hPa zonal wind u (u850), zonal wind vertical shear [u shear, defined by the difference between u850 and 200-hPa zonal wind (u200)], 850-hPa relative vorticity and divergence, and model SSW pattern skill based on these multimodel simulations. Model skill in simulating these summer mean patterns is derived by calculating pattern correlations of these fields with their observational counterparts over the WNP domain of 0°–30°N, 100°–160°E. As shown in Table 2, model skill in simulating the summer mean rainfall, u850, u shear, and 850-hPa vorticity patterns are not significantly correlated to model SSW pattern skill.[2] Particularly noteworthy is the great correlation (0.60) between model skill in summer mean 850-hPa divergence pattern and SSW skill (Table 2 and Fig. 7a), suggesting that energy accumulation resulting from low-level convergence associated with the monsoon trough could indeed play a critical role for the observed SSW pattern as previously suggested (e.g., Lau and Lau 1990; Sobel and Bretherton 1999; Kuo et al. 2001).

Figure 8 further illustrates summer mean divergence (shaded) and wind (vectors) patterns at 850 hPa along with STD of reconstructed rainfall anomalies (PR_{rec}) based on the two leading EEOFs of 3–8-day rainfall over the WNP (contours) for observations and composites based on good and bad SSW models. Again, the observed low-level circulation over the WNP is characterized by the confluent zone associated with the monsoon trough, formed by the monsoon westerlies and easterlies of the Pacific subtropical high (Fig. 8a). A southeast–northwest-tilted convergence maximum center is evident to the east of the Philippines. Meanwhile, the observed SSW activity center is largely collocated

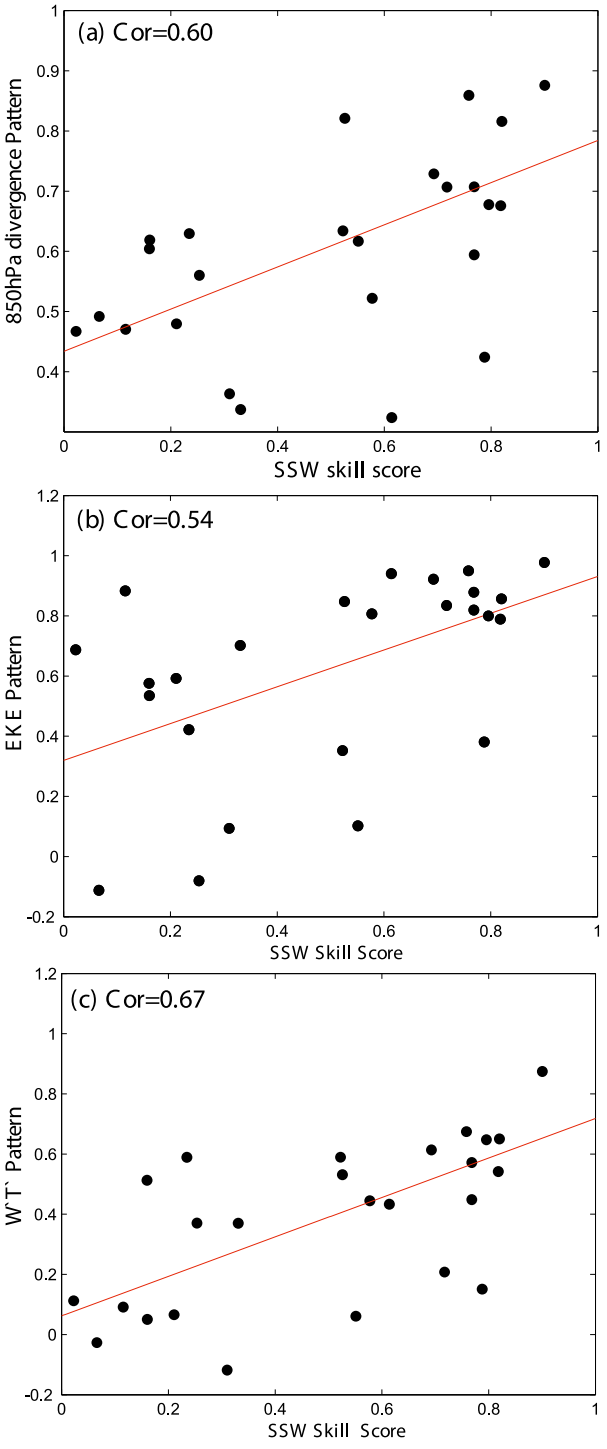

FIG. 7. Scatterplots between SSW skill scores and model skill for summer mean patterns of (a) 850-hPa divergence, (b) vertically averaged EKE, (c) and $\overline{w'T'}$, across 27 GCM simulations. The red line in each panel denotes linear fit by least squares means. Correlation coefficient is also displayed in each panel.

[2] Since output from 25 GCMs is used for calculations, a 95% significance level corresponds to a correlation coefficient of 0.36 based on a one-tailed Student's t test.

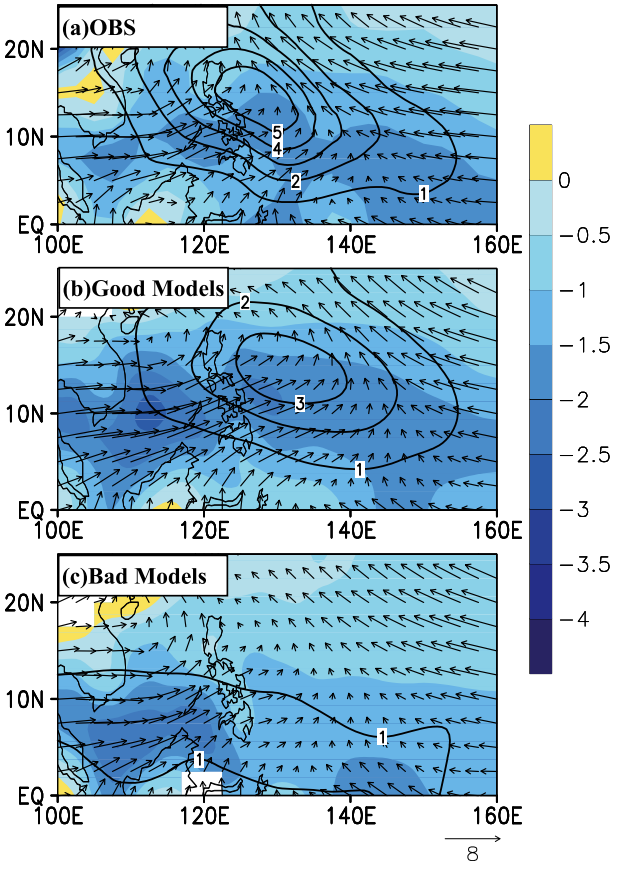

FIG. 8. Standard deviations of EEOF-based PR_{rec} (mm day^{-1}; contours), 850-hPa divergence (10^{-5} s^{-1}; shaded), and winds (m s^{-1}; vectors, see the scale vector at bottom right) for (a) the observations, (b) good model, and (c) bad model composite.

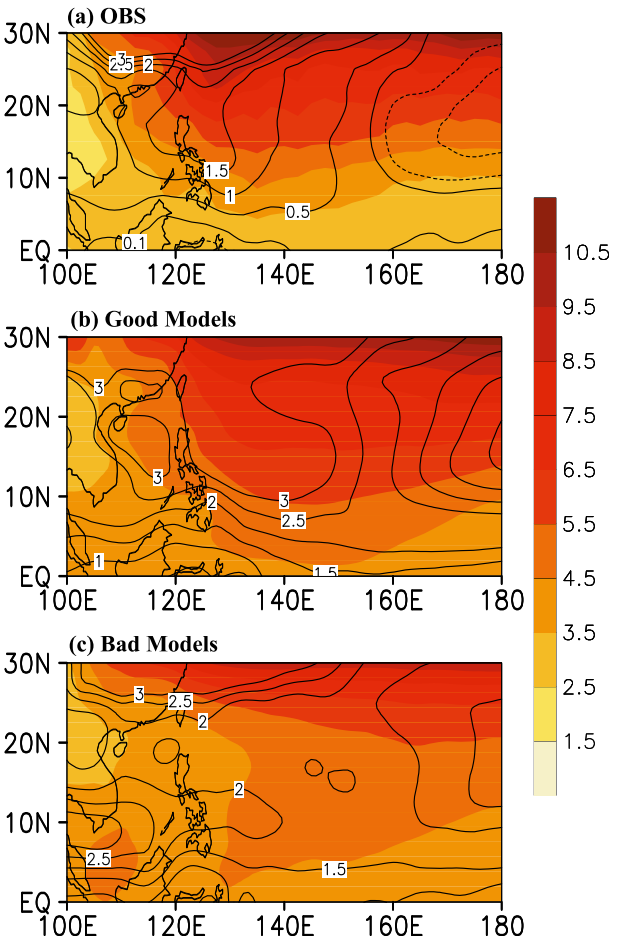

FIG. 9. Vertically averaged EKE (m^2 s^{-2}; contour) and $\overline{w'T'}$ (Pa s^{-1} K; shaded) for (a) the observations, (b) good model, and (c) bad model composite.

with the convergent zone, slightly displaced to the north of maximum convergence. These prominent observed features, including 850-hPa wind and divergence patterns, as well as the SSW activity maximum center, are realistically simulated by good SSW model composites in general (Fig. 8b). In contrast, convergent low-level circulations of the monsoon trough are not well simulated in bad SSW model composites. The easterlies associated with the Pacific subtropical high are much weaker over the WNP, leaving the convergent region of the monsoon trough not as well organized as in the observations (Fig. 8c). Instead, the strongest convergence zone is found over the South China Sea to the west of the Philippines and western equatorial Pacific near 140°E, in correspondence to the southward shift of weaker SSW activity centers in bad SSW model composites (Fig. 8c). Therefore, in agreement with the high correlations between model skill for summer mean 850-hPa divergence pattern and model skill for the SSW pattern, results shown in Fig. 8 further suggest that realistic simulations of lower-tropospheric convergent flow associated with the monsoonal trough could be crucial for the realistic simulation of the SSW pattern over the WNP.

To gain additional insights into processes for good SSW simulations in GCMs, model skill in simulating summer mean patterns of vertically averaged synoptic EKE [defined as $0.5\overline{(u'^2 + v'^2)}$] and the conversion from EAPE to EKE $\overline{w'T'}$ over the WNP is also correlated against model SSW skill across GCM simulations. Here u', v', w', and T' are 3–8-day bandpass-filtered fields of zonal winds, meridional winds, pressure level vertical velocity, and temperature, respectively. Results suggest that model skill in both vertically averaged EKE and $\overline{w'T'}$ patterns are significantly correlated with model SSW skill (Table 2 and Figs. 7b,c). To further demonstrate this, summer mean patterns of vertically averaged EKE and $\overline{w'T'}$ based on the observations and good and bad SSW model composites are further illustrated in Fig. 9. In accord with the

TABLE 3. Correlations between summer mean rainfall, STDs of 3–8-day-filtered rainfall and SSW leading EEOF-based reconstructed rainfall anomalies, and vertically averaged EKE over the WNP core region. All correlations are significant at a 99% level.

	STD_3–8d	STD_rec	EKE
Summer rainfall	0.68	0.74	0.60
STD_3–8d	—	0.88	0.77
STD_rec	—	—	0.82

observed SSW activity over the WNP (see contours in Fig. 8a), a local maximum in EKE is also evident (contours in Fig. 9a), along with strong conversions from EAPE to EKE (shaded in Fig. 9a). The observed local vertically averaged EKE center along with strong $\overline{w'T'}$ over the WNP are well simulated in good SSW models (Fig. 9b) but not in the bad SSW model composite (Fig. 9c). These results suggest that, in addition to the energy source associated with the barotropic conversion by the low-level convergence over the monsoon trough, EKE generation by conversion from EAPE could also play a critical role for realistic simulations of SSW in climate models.

b. *Factors associated with model SSW amplitude*

In this part, we proceed to examine possible large-scale factors in regulating model SSW amplitude based on multimodel simulations. We first define a core region over the WNP (5°–25°N, 110°–150°E) to measure the amplitude of the SSW. As shown by Table 3, three different measurements of SSW amplitude—namely, the STDs of the 3–8-day-filtered rainfall (STD_3–8d), the EEOF-based reconstructed rainfall (STD_rec), and the EKE averaged over the same core region—are highly correlated with each other. Also, note that the SSW amplitude over the WNP measured by all three approaches exhibits significant correlation to summer mean rainfall intensity (Table 3). The close association between the STD_rec and vertically averaged EKE over the WNP core region is further displayed by Fig. 10, with a correlation of 0.82. In the following, the EKE averaged over the WNP core region in each model will be employed as the primary index for model SSW amplitude by considering that budget analyses based on the EKE equation could provide further understanding of energetics associated with SSW activity as in many previous studies (e.g., Lau and Lau 1992; Maloney and Dickinson 2003; Rydbeck and Maloney 2014; Fukutomi et al. 2016). While detailed analyses of the EKE budget based on these multimodel simulations are still under investigation and will be reported in a separate

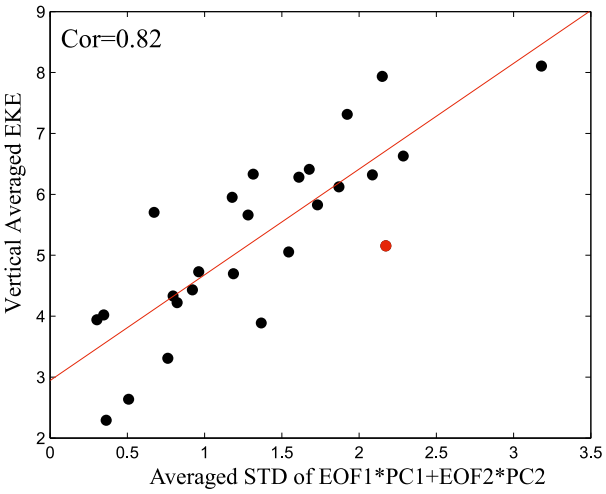

FIG. 10. Scatterplots between the vertically averaged EKE intensity ($m^2 s^{-2}$) over the WNP core region and the STD of the EEOF-based reconstructed rainfall anomalies (mm day^{-1}) in model simulations. The red line denotes the linear fit by least squares means, and the red dot represents the observations. The correlation coefficient is also displayed.

manuscript, in this study we attempt to identify critical processes which regulate model EKE amplitude by conducting correlations of several large-scale factors onto the SSW amplitude across these multimodel simulations.

Table 4 shows correlation coefficients of several summer mean variables, including u shear, 850-hPa vorticity and divergence, and vertically averaged $\overline{w'T'}$ against EKE over the WNP core region in model simulations. While vertical shear of mean zonal wind does not show significant correlation with model SSW amplitude, three other variables, including 850-hPa divergence and vertically averaged $\overline{w'T'}$, are highly correlated with SSW amplitude. The close associations between EKE amplitude and 850-hPa divergence and vertically averaged $\overline{w'T'}$ in simulations are further clearly evident in Fig. 11. These results suggest that more effective EKE generation by barotropic conversions associated with stronger

TABLE 4. Correlations of vertically averaged EKE and amplitude of model u shear, 850 hPa relative vorticity and divergence, and vertically averaged $\overline{w'T'}$ across multimodel simulations. All these variables are averaged over the WNP core region. Significant correlations at a 99% confidence level are indicated by asterisks.

Model variable	Correlation
u shear (u850 − u200)	−0.31
850-hPa relative vorticity	0.47*
850-hPa divergence	−0.71*
$\overline{w'T'}$	−0.83*

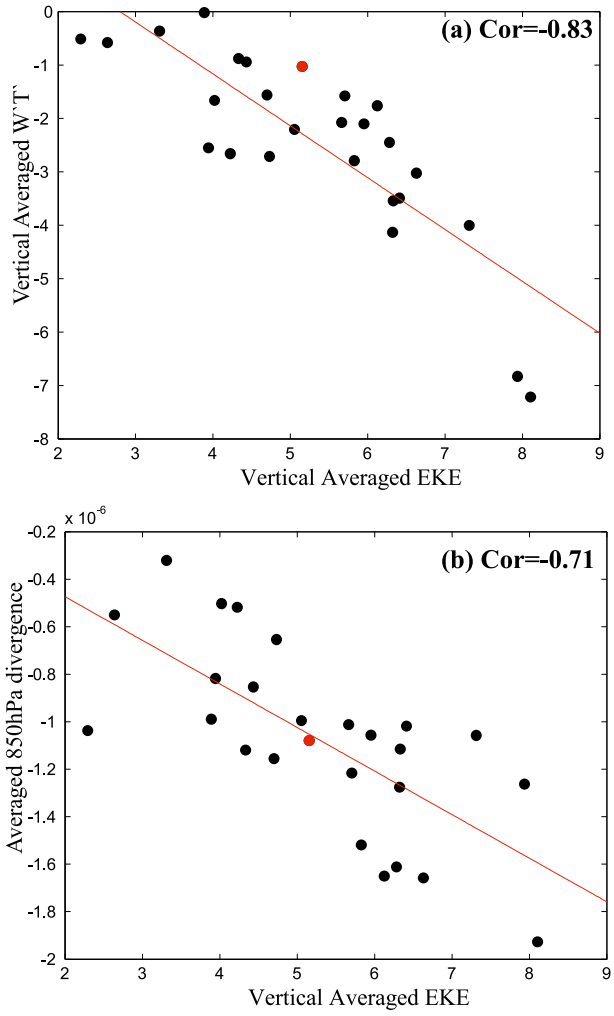

FIG. 11. Scatterplot between the intensity of (top) vertically averaged $\overline{w'T'}$ and (bottom) 850-hPa divergence and amplitude of vertically averaged EKE across model simulations. The red dot in each panel represents the observations. The red line denotes the linear fit by least squares means. Correlation coefficients are also displayed.

low-level cyclonic and convergent flow, as well as energy conversion from EAPE to EKE, will lead to stronger SSWs in a model. Further analysis suggests that generation of the EAPE associated with the SSWs is largely due to the covariance term between perturbation convective heating and temperature (figure not shown).

6. Modulation of the MJO on SSW activity over the WNP in climate models

As previously discussed, it has been widely reported that various large-scale climate variability modes, including the MJO, exert significant modulations on SSW activity over the WNP. In this section, taking the MJO as an example, we further examine how modulations of SSW activity by the MJO are depicted in climate models.

To provide an objective evaluation of model performance in simulating the boreal summer MJO over the WNP, a similar EEOF analysis approach is conducted as for the SSW described in section 4a, except that evolution patterns of 20–100-day bandpass-filtered rainfall from day −15 to day +15 with an interval of 5 days are applied for the EEOF. Also similarly, leading summer MJO modes based on both observations and model simulations are derived by lag regressions of reconstructed rainfall anomalies based on EEOF1 and EEOF2 against an averaged value over a 5° × 5° box centered at 15°N, 130°E. Each model skill in representing the summer MJO is then derived by pattern correlation of the evolution of 2D rainfall patterns over the area of 0°–30°N, 100°–160°E, from day −15 to day +15 at an interval of 5 days based on these lag-regressed patterns between model simulations and observations, in a similar way when evaluating model skill for SSW patterns.

Figure 12 illustrates model pattern correlation scores for the summer MJO over the WNP. Again, seven GCMs showing the highest pattern correlations are selected as good MJO models: ACCESS1.0, CAM5, CFSv2, EC-EARTH3, MRI_AGCM3, Pusan National University Climate Forecast System (PNU-CFS), and TAMU-CAM4. Similarly, seven models with the lowest correlations are selected as bad MJO models. Evolution patterns of the 2D rainfall anomalies of the leading summer MJO mode over the WNP based on the observations, as well as good and bad model composites, are further shown in Fig. 13. The observed boreal summer MJO is characterized by the eastward shift of enhanced convection crossing the Maritime Continent (from day −15 to day −10), then northwestward propagation of equatorial convection toward southeastern China (from day −10 to day +15 in Fig. 13, left). These observed features are generally well captured in good model simulations (Fig. 13, center). As a contrast, while the northwestward movement of the MJO convection over the WNP is captured in bad model simulations, these models fail to capture the eastward migration of tropical convection during the early evolution (Fig. 13, right). Meanwhile, convective organization in bad MJO models exhibits a southwest–northeast tilt rather than a slightly southeast–northwest tilt in the observations. Since our work mainly focuses on the SSW over the WNP, comprehensive evaluation of model skill for summer MJO is beyond the scope of this study and will be reported separately (e.g., Neena et al. 2016).

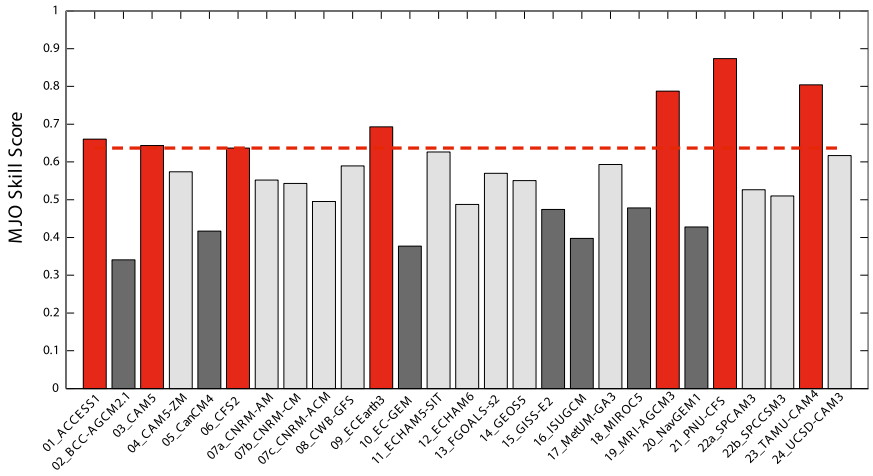

FIG. 12. MJO skill scores in GCMs based on pattern correlations of lag-regressed rainfall anomalies associated with simulated leading MJO mode over the WNP against the observational counterpart. Red (dark gray) bars denote the top (bottom) 25% GCMs in simulating the summer MJO pattern over the WNP.

As previously mentioned, we are particularly interested in examining how MJO modulation on SSWs over the WNP is simulated by climate models. For this purpose, four GCMs (ACCESS1.0, CAM5, EC-EARTH3, and TAMU-CAM4), which exhibit high skill scores for both summer MJO and SSW modes over the WNP, are selected for the following analyses. First, two opposite MJO phases over the WNP are defined by the STD of rainfall anomalies over the domain of 12.5°–17.5°N, 127.5°–132.5°E, based on the reconstructed rainfall anomalies using EEOF1 and EEOF2 of the boreal summer MJO mode for both observations and the above four selected GCMs. The enhanced phase of the WNP MJO is then defined by the period when the area-averaged rainfall anomalies exceed 1.5 STD. Similarly, suppressed MJO phases are defined by periods when domain-averaged rainfall anomalies are less than −1.5 STD. The SSW amplitude for the enhanced and suppressed MJO phases can then be calculated by STDs of SSW EEOF-based reconstructed rainfall anomalies for both observations and GCM simulations. Meanwhile, spatial SSW patterns during the two MJO phases can be derived by the lag-0 regressions of the reconstructed rainfall anomalies associated with the leading SSW modes onto a base point (15°N, 130°E).

Figure 14 illustrates the amplitude of SSWs during enhanced and suppressed MJO phases in the observations and the four-GCM composite. Strong MJO modulation on the amplitude of SSWs over the WNP is readily seen in the observations; the SSW amplitude is greatly increased (damped) during the enhanced (suppressed) MJO phases (Figs. 14a,b), in agreement with previous studies (e.g., Maloney and Dickinson 2003; Hsu and Li 2011). Interestingly, the observed strong modulation of the SSW amplitude by the MJO is well simulated in the four selected GCMs (Figs. 14c,d), although the simulated SSW amplitude is systemically weaker than the observed for both the enhanced and suppressed MJO phases.

Figure 15 further portrays SSW patterns during the enhanced and suppressed MJO phases for observations and the GCM composite. While the SSW wave patterns are similar during enhanced and suppressed MJO phases in the observations, the amplitude of the southeast–northwest-aligned activity center is much stronger during the enhanced MJO phases than that during the suppressed phases (Figs. 15a,b). The modulation in amplitude of SSW patterns by the MJO is also well simulated in the four model simulations (Figs. 15c,d). Detailed processes associated with MJO simulations on the SSW amplitude are under investigation by conducting EKE budget analyses for different MJO phases, which could provide further insights into detailed processes associated with large-scale modulations of SSW activity.

7. Summary

During boreal summer, vigorous synoptic-scale wave (SSW) activity is observed over the WNP, often characterized by southeast–northwest-oriented wave trains along the monsoon trough. These SSWs not only have significant impacts on regional extreme rainfall events but also serve as critical precursors for formation of tropical cyclones over the WNP. Meanwhile, collective

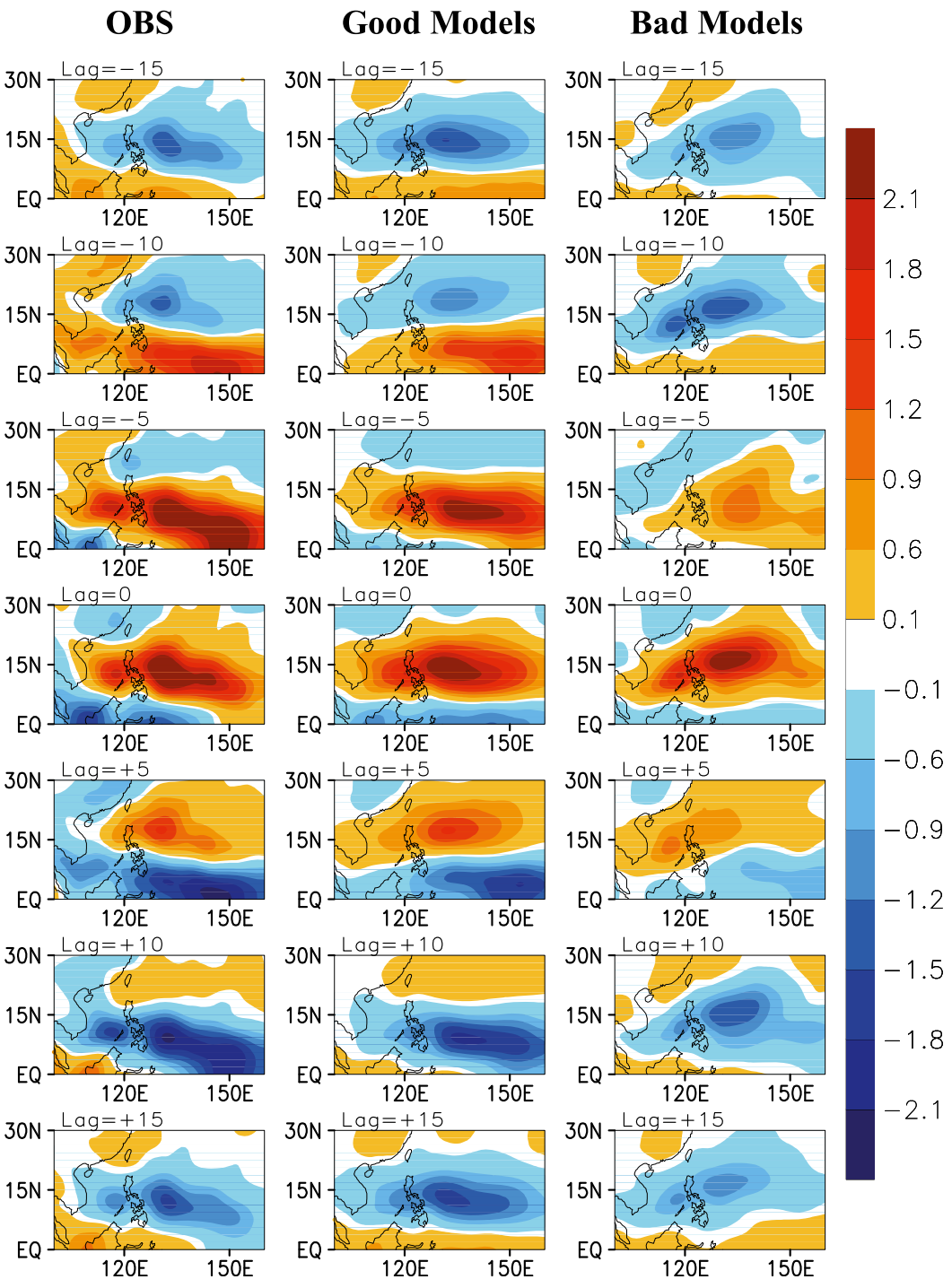

FIG. 13. Evolution patterns of leading summer MJO mode (mm day^{-1}) over the WNP from day −15 to day 15 for (left) the observations and composite based on seven (center) good and (right) bad model simulations.

impacts by SSWs may also play an active role in sustaining low-frequency variability over the WNP. Previous studies suggest that preference of SSWs over the WNP is intimately associated with local monsoonal circulation (Lau and Lau 1990; Zehr 1992; Chang et al. 1996; Sobel and Bretherton 1999; Li 2006), and the SSW activity can be significantly modulated by large-scale climate variability modes such as the MJO.

In spite of its prominent role for regional weather and climate, modeling studies on SSWs over the WNP

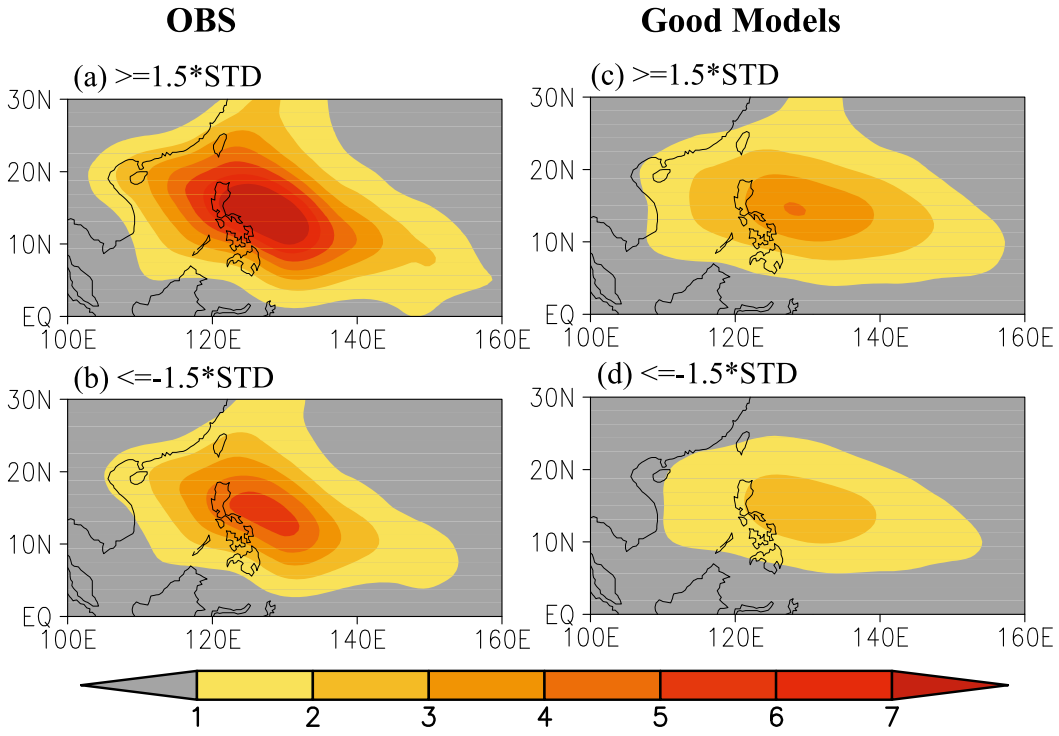

FIG. 14. Standard deviations of EEOF-based reconstructed rainfall (mm day^{-1}) of the leading SSW mode in (a),(b) the observations and (c),(d) model composite based on the four selected models (ACCESS1.0, CAM5, EC-EARTH3, and TAMU-CAM4) during (top) enhanced and (bottom) suppressed MJO phases.

are rather limited. In this study, by analyzing output from participants of 27 model simulations in the recent MJOTF/GASS MJO global model evaluation project, a comprehensive survey on model skill in representing SSWs over the WNP is conducted. Results illustrate that it is greatly challenging for present-day GCMs to realistically represent the observed leading SSW mode over the WNP. While many models are able to capture the southeast–northwest-slanted wave trains over the WNP, GCMs exhibit a variety of deficiencies in representing the observed SSW mode, including the amplitude, maximum activity center, spatial scales, and orientation of the wave train axis. Only 2 models among the 27 GCMs examined, ACCESS1.0 and GISS-E2, generally well simulate both the intensity and spatial pattern of observed SSWs over the WNP.

Plausible key processes responsible for realistic simulations of SSWs, including their spatial pattern and intensity, are further explored based on these multimodel simulations. It is found that GCM skill in representing the spatial pattern of SSWs over the WNP is highly correlated to model skill in simulating the summer mean 850-hPa convergence pattern associated with the WNP monsoon trough, in agreement with previous studies that energy accumulation by the background monsoon confluent circulation is critical in sustaining observed SSWs (e.g., Sobel and Bretherton 1999; Kuo et al. 2001; Tam and Li 2006). Additionally, realistic simulations of the SSW pattern in GCMs also benefit from high-quality simulations of conversion processes from eddy available potential energy (EAPE) to eddy kinetic energy (EKE), also consistent with previous studies that EAPE, generated by cumulus condensational heating, plays a critical role in sustaining SSWs over the WNP (e.g., Lau and Lau 1990; Maloney and Dickinson 2003). On the other hand, the intensity of SSWs, as represented by vertically averaged EKE averaged over a core region of the WNP, is found to be highly correlated with the amplitude of vorticity, divergence at 850 hPa, and vertically averaged $\overline{w'T'}$ across these multimodel simulations, further suggesting critical roles of barotropic conversions and conversion from EAPE to EKE in energizing the WNP SSW.

Modulation of SSW activity over the WNP by the MJO is further examined based on model simulations from the four selected GCMs that well simulate both the SSW and summer MJO patterns over the WNP. The results illustrate that the observed strong modulations of the SSW

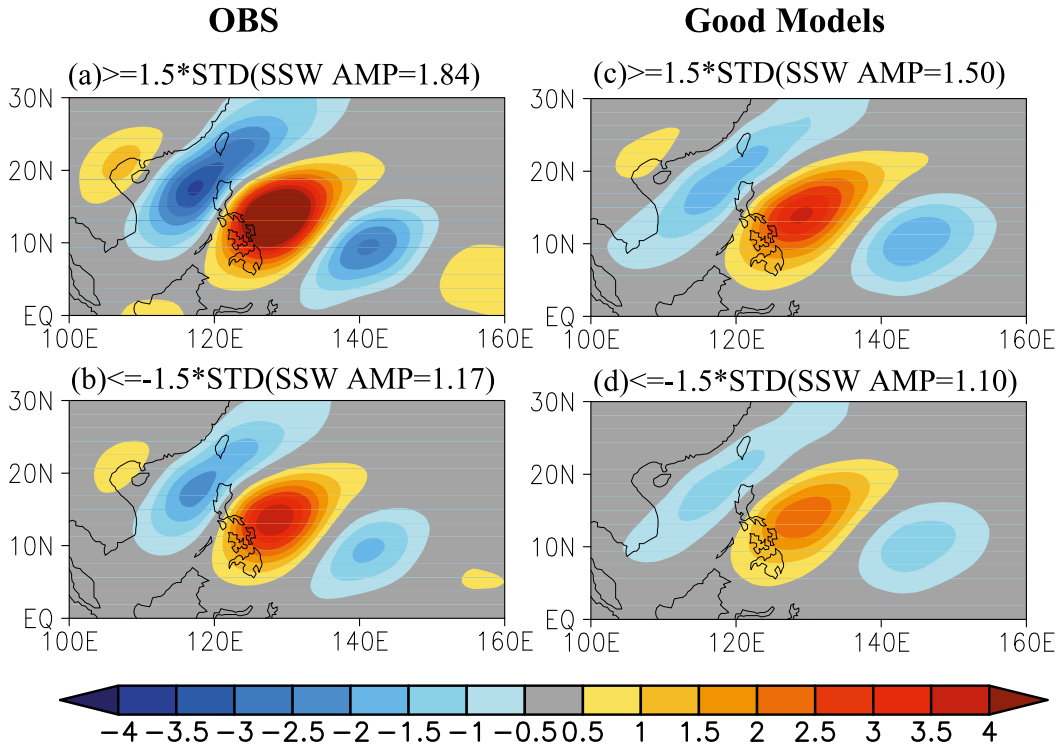

FIG. 15. (a),(b) Observed and (c),(d) simulated spatial patterns (mm day^{-1}) of the WNP SSW mode during (top) active and (bottom) suppressed MJO phases. Model simulations are based on composite from the four selected GCMs as indicated in Fig. 14.

intensity by the MJO are able to be captured in these GCMs; namely, during the local MJO active phases, SSW activity is greatly enhanced while much weaker SSW activity is found during the MJO inactive phases.

While results in this study are largely in agreement with previous observational studies on critical processes associated with the WNP SSWs from a modeling perspective, these process-oriented diagnoses based on multimodel simulations provide critical validation of these processes and also important guidance for model development, particularly considering significant model deficiencies in current climate models in representing the WNP SSW mode. Moreover, a budget analysis of the EKE equation based on model simulations is currently being conducted, which can provide further insight into detailed processes responsible for the energetics of the WNP SSW.

Acknowledgments. We thank modeling groups for making available their model output through the MJOTF/GASS MJO project. We also thank insightful comments from K.-H. Seo and two other reviewers, which greatly helped improve this manuscript. H. Zhao thanks the support from the National Natural Science Foundation of China (Grant 41305050) and the Priority Academic Program Development of Jiangsu Higher Education Institutions (PAPD). L. Wu acknowledges the National Basic Research Program of China (2013CB430103 and 2015CB452803), the National Natural Science Foundation of China (Grant 41275093), and the project of the specially appointed professorship of Jiangsu Province. X. Jiang acknowledges support by the U.S. NSF Climate and Large-Scale Dynamics Program under Award AGS-1228302 and the NOAA Climate Program Office under Awards NA12OAR4310075, NA15OAR4310098, and NA15OAR4310177.

REFERENCES

Aiyyer, A. R., and J. Molinari, 2003: Evolution of mixed Rossby–gravity waves in idealized MJO environments. *J. Atmos. Sci.*, **60**, 2837–2855, doi:10.1175/1520-0469(2003)060<2837:EOMRWI>2.0.CO;2.

Benedict, J. J., and D. A. Randall, 2007: Observed characteristics of the MJO relative to maximum rainfall. *J. Atmos. Sci.*, **64**, 2332–2354, doi:10.1175/JAS3968.1.

Chang, C. P., V. F. Morris, and J. M. Wallace, 1970: A statistical study of easterly waves in the western Pacific: July–December 1964. *J. Atmos. Sci.*, **27**, 195–201, doi:10.1175/1520-0469(1970)027<0195:ASSOEW>2.0.CO;2.

——, J. M. Chen, P. A. Harr, and L. E. Carr, 1996: Northwestward-propagating wave patterns over the tropical western North

Pacific during summer. *Mon. Wea. Rev.*, **124**, 2245–2266, doi:10.1175/1520-0493(1996)124<2245:NPWPOT>2.0.CO;2.

Chen, G., 2012: A comparison of the transition of equatorial waves between two types of ENSO events in a multilevel model. *J. Atmos. Sci.*, **69**, 2364–2378, doi:10.1175/JAS-D-11-0292.1.

——, and R. Huang, 2009: Interannual variations in mixed Rossby–gravity waves and their impacts on tropical cyclogenesis over the western North Pacific. *J. Climate*, **22**, 535–549, doi:10.1175/2008JCLI2221.1.

——, and C. Chou, 2014: Joint contribution of multiple equatorial waves to tropical cyclogenesis over the western North Pacific. *Mon. Wea. Rev.*, **142**, 79–93, doi:10.1175/MWR-D-13-00207.1.

Chen, T.-C., and S.-P. Weng, 1996: Some effects of the intraseasonal oscillation on the equatorial waves over the western tropical Pacific–South China Sea region during the northern summer. *Mon. Wea. Rev.*, **124**, 751–756, doi:10.1175/1520-0493(1996)124<0751:SEOTIO>2.0.CO;2.

——, J.-D. Tsay, M.-C. Yen, and J. Matsumoto, 2012: Interannual variation of the late fall rainfall in central Vietnam. *J. Climate*, **25**, 392–413, doi:10.1175/JCLI-D-11-00068.1.

Dee, D. P., and Coauthors, 2011: The ERA-Interim reanalysis: Configuration and performance of the data assimilation system. *Quart. J. Roy. Meteor. Soc.*, **137**, 553–597, doi:10.1002/qj.828.

DeMott, C. A., C. Stan, and D. A. Randall, 2012: Northward propagation mechanisms of the boreal summer intraseasonal oscillation in the ERA-Interim and SP-CCSM. *J. Climate*, **26**, 1973–1992, doi:10.1175/JCLI-D-12-00191.1.

——, ——, ——, and M. D. Branson, 2014: Intraseasonal variability in coupled GCMs: The roles of ocean feedbacks and model physics. *J. Climate*, **27**, 4970–4995, doi:10.1175/JCLI-D-13-00760.1.

Dickinson, M., and J. Molinari, 2002: Mixed Rossby–gravity waves and western Pacific tropical cyclogenesis. Part I: Synoptic evolution. *J. Atmos. Sci.*, **59**, 2183–2196, doi:10.1175/1520-0469(2002)059<2183:MRGWAW>2.0.CO;2.

Dunkerton, T. J., 1993: Observation of 3–6-day meridional wind oscillations over the tropical Pacific, 1973–1992: Vertical structure and interannual variability. *J. Atmos. Sci.*, **50**, 3292–3307, doi:10.1175/1520-0469(1993)050<3292:OODMWO>2.0.CO;2.

——, and M. P. Baldwin, 1995: Observation of 3–6-day meridional wind oscillations over the tropical Pacific, 1973–1992: Horizontal structure and propagation. *J. Atmos. Sci.*, **52**, 1585–1601, doi:10.1175/1520-0469(1995)052<1585:OODMWO>2.0.CO;2.

Frierson, D. M. W., D. Kim, I.-S. Kang, M.-I. Lee, and J. Lin, 2011: Structure of AGCM-simulated convectively coupled Kelvin waves and sensitivity to convective parameterization. *J. Atmos. Sci.*, **68**, 26–45, doi:10.1175/2010JAS3356.1.

Fukutomi, Y., C. Kodama, Y. Yamada, A. T. Noda, and M. Satoh, 2016: Tropical synoptic-scale wave disturbances over the western Pacific simulated by a global cloud-system resolving model. *Theor. Appl. Climatol.*, **124**, 737–755, doi:10.1007/s00704-015-1456-4.

Holland, G. J., 1995: Scale interaction in the western Pacific monsoon. *Meteor. Atmos. Phys.*, **56**, 57–79, doi:10.1007/BF01022521.

Hsu, P.-C., and T. Li, 2011: Interactions between boreal summer intraseasonal oscillations and synoptic-scale disturbances over the western North Pacific. Part II: Apparent heat and moisture sources and eddy momentum transport. *J. Climate*, **24**, 942–961, doi:10.1175/2010JCLI3834.1.

——, ——, and C.-H. Tsou, 2011: Interactions between boreal summer intraseasonal oscillations and synoptic-scale disturbances over the western North Pacific. Part I: Energetics diagnosis. *J. Climate*, **24**, 927–941, doi:10.1175/2010JCLI3833.1.

Huang, P., C. Chou, and R. Huang, 2013: The activity of convectively coupled equatorial waves in CMIP3 global climate models. *Theor. Appl. Climatol.*, **112**, 697–711, doi:10.1007/s00704-012-0761-4.

Huffman, G. J., R. F. Adler, B. Rudolf, U. Schneider, and P. R. Keehn, 1995: Global precipitation estimates based on a technique for combining satellite-based estimates, rain gauge analysis, and NWP model precipitation information. *J. Climate*, **8**, 1284–1295, doi:10.1175/1520-0442(1995)008<1284:GPEBOA>2.0.CO;2.

Hung, M.-P., J.-L. Lin, W. Wang, D. Kim, T. Shinoda, and S. J. Weaver, 2013: MJO and convectively coupled equatorial waves simulated by CMIP5 climate models. *J. Climate*, **26**, 6185–6214, doi:10.1175/JCLI-D-12-00541.1.

Jiang, X., and Coauthors, 2012: Simulation of the intraseasonal variability over the eastern Pacific ITCZ in climate models. *Climate Dyn.*, **39**, 617–636, doi:10.1007/s00382-011-1098-x.

——, and Coauthors, 2015: Vertical structure and physical processes of the Madden-Julian oscillation: Exploring key model physics in climate simulations. *J. Geophys. Res. Atmos.*, **120**, 4718–4748, doi:10.1002/2014JD022375.

Khairoutdinov, M., C. DeMott, and D. Randall, 2008: Evaluation of the simulated interannual and subseasonal variability in an AMIP-style simulation using the CSU multiscale modeling framework. *J. Climate*, **21**, 413–431, doi:10.1175/2007JCLI1630.1.

Kim, J.-H., C.-H. Ho, H.-S. Kim, and W. Choi, 2012: 2010 western North Pacific typhoon season: Seasonal overview and forecast using a track-pattern-based model. *Wea. Forecasting*, **27**, 730–743, doi:10.1175/WAF-D-11-00109.1.

Klingaman, N. P., and Coauthors, 2015: Vertical structure and physical processes of the Madden-Julian oscillation: Linking hindcast fidelity to simulated diabatic heating and moistening. *J. Geophys. Res. Atmos.*, **120**, 4690–4717, doi:10.1002/2014JD022374.

Kuo, H. C., J. H. Chen, R. T. Williams, and C. P. Chang, 2001: Rossby waves in zonally opposing mean flow: Behavior in northwest Pacific summer monsoon. *J. Atmos. Sci.*, **58**, 1035–1050, doi:10.1175/1520-0469(2001)058<1035:RWIZOM>2.0.CO;2.

Lau, K. H., and N. C. Lau, 1990: Observed structure and propagation characteristics of tropical summertime synoptic scale disturbances. *Mon. Wea. Rev.*, **118**, 1888–1913, doi:10.1175/1520-0493(1990)118<1888:OSAPCO>2.0.CO;2.

——, and ——, 1992: The energetics and propagation dynamics of tropical summertime synoptic-scale disturbances. *Mon. Wea. Rev.*, **120**, 2523–2539, doi:10.1175/1520-0493(1992)120<2523:TEAPDO>2.0.CO;2.

Li, R. C. Y., W. Zhou, and T. Li, 2014: Influences of the Pacific–Japan teleconnection pattern on synoptic-scale variability in the western North Pacific. *J. Climate*, **27**, 140–154, doi:10.1175/JCLI-D-13-00183.1.

Li, T., 2006: Origin of the summertime synoptic-scale wave train in the western North Pacific. *J. Atmos. Sci.*, **63**, 1093–1102, doi:10.1175/JAS3676.1.

——, 2014: Recent advance in understanding the dynamics of the Madden-Julian oscillation. *J. Meteor. Res.*, **28**, 1–33, doi:10.1007/s13351-014-3087-6.

——, and B. Fu, 2006: Tropical cyclogenesis associated with Rossby wave energy dispersion of a preexisting typhoon. Part I: Satellite data analyses. *J. Atmos. Sci.*, **63**, 1377–1389, doi:10.1175/JAS3692.1.

——, ——, X. Ge, B. Wang, and M. Peng, 2003: Satellite data analysis and numerical simulation of tropical cyclone formation. *Geophys. Res. Lett.*, **30**, 2122, doi:10.1029/2003GL018556.

——, X. Ge, B. Wang, and Y. Zhu, 2006: Tropical cyclogenesis associated with Rossby wave energy dispersion of a preexisting typhoon. Part II: Numerical simulations. *J. Atmos. Sci.*, **63**, 1390–1409, doi:10.1175/JAS3693.1.

Liebmann, B., and H. H. Hendon, 1990: Synoptic-scale disturbances near the equator. *J. Atmos. Sci.*, **47**, 1463–1479, doi:10.1175/1520-0469(1990)047<1463:SSDNTE>2.0.CO;2.

——, ——, and J. D. Glick, 1994: The relationship between tropical cyclones of the western Pacific and Indian Oceans and the Madden-Julian oscillation. *J. Meteor. Soc. Japan*, **72**, 401–412.

Lin, J.-L., and Coauthors, 2006: Tropical intraseasonal variability in 14 IPCC AR4 climate models. Part I: Convective signals. *J. Climate*, **19**, 2665–2690, doi:10.1175/JCLI3735.1.

——, M. I. Lee, D. Kim, I. S. Kang, and D. M. W. Frierson, 2008: The impacts of convective parameterization and moisture triggering on AGCM-simulated convectively coupled equatorial waves. *J. Climate*, **21**, 883–909, doi:10.1175/2007JCLI1790.1.

Liu, K. S., and J. C. L. Chan, 2013: Inactive period of western North Pacific tropical cyclone activity in 1998–2011. *J. Climate*, **26**, 2614–2630, doi:10.1175/JCLI-D-12-00053.1.

Maloney, E. D., and D. L. Hartmann, 2001: The Madden–Julian oscillation, barotropic dynamics, and North Pacific tropical cyclone formation. Part I: Observations. *J. Atmos. Sci.*, **58**, 2545–2558, doi:10.1175/1520-0469(2001)058<2545:TMJOBD>2.0.CO;2.

——, and M. J. Dickinson, 2003: The intraseasonal oscillation and the energetics of summertime tropical western North Pacific synoptic-scale disturbances. *J. Atmos. Sci.*, **60**, 2153–2168, doi:10.1175/1520-0469(2003)060<2153:TIOATE>2.0.CO;2.

Moncrieff, M. W., D. E. Waliser, M. J. Miller, M. A. Shapiro, G. R. Asrar, and J. Caughey, 2012: Multiscale convective organization and the YOTC virtual global field campaign. *Bull. Amer. Meteor. Soc.*, **93**, 1171–1187, doi:10.1175/BAMS-D-11-00233.1.

Nakazawa, T., 1988: Tropical super clusters within intraseasonal variations over the western Pacific. *J. Meteor. Soc. Japan*, **66**, 823–839.

Neena, J. M., D. Waliser, and X. Jiang, 2016: Model performance metrics and process diagnostics for boreal summer intraseasonal variability. *Climate Dyn.*, doi:10.1007/s00382-016-3166-8, in press.

Petch, J., D. Waliser, X. Jiang, P. Xavier, and S. Woolnough, 2011: A global model inter-comparison of the physical processes associated with the Madden-Julian oscillation. *GEWEX News*, No. 21, International GEWEX Project Office, Silver Spring, MD, 3–5.

Pritchard, M. S., and C. S. Bretherton, 2014: Causal evidence that rotational moisture advection is critical to the superparameterized Madden–Julian oscillation. *J. Atmos. Sci.*, **71**, 800–815, doi:10.1175/JAS-D-13-0119.1.

Randall, D., M. Khairoutdinov, A. Arakawa, and W. Grabowski, 2003: Breaking the cloud parameterization deadlock. *Bull. Amer. Meteor. Soc.*, **84**, 1547–1564, doi:10.1175/BAMS-84-11-1547.

Reed, R. J., and E. E. Recker, 1971: Structure and properties of synoptic-scale wave disturbances in the equatorial western Pacific. *J. Atmos. Sci.*, **28**, 1117–1133, doi:10.1175/1520-0469(1971)028<1117:SAPOSS>2.0.CO;2.

Reynolds, R. W., N. A. Rayner, T. M. Smith, D. C. Stokes, and W. Wang, 2002: An improved in situ and satellite SST analysis for climate. *J. Climate*, **15**, 1609–1625, doi:10.1175/1520-0442(2002)015<1609:AIISAS>2.0.CO;2.

Riehl, H., 1945: Waves in the easterlies and the polar front in the tropics. University of Chicago Dept. of Meteorology Miscellaneous Rep. 17, 79 pp.

Ritchie, E. A., and G. J. Holland, 1997: Scale interactions during the formation of Typhoon Irving. *Mon. Wea. Rev.*, **125**, 1377–1396, doi:10.1175/1520-0493(1997)125<1377:SIDTFO>2.0.CO;2.

——, and ——, 1999: Large-scale patterns associated with tropical cyclogenesis in the western Pacific. *Mon. Wea. Rev.*, **127**, 2027–2043, doi:10.1175/1520-0493(1999)127<2027:LSPAWT>2.0.CO;2.

Rydbeck, A. V., and E. D. Maloney, 2014: Energetics of east Pacific easterly waves during intraseasonal events. *J. Climate*, **27**, 7603–7621, doi:10.1175/JCLI-D-14-00211.1.

Seo, K.-H., J.-H. Choi, and S.-D. Han, 2012: Factors for the simulation of convectively coupled Kelvin waves. *J. Climate*, **25**, 3495–3514, doi:10.1175/JCLI-D-11-00060.1.

Serra, Y. L., X. Jiang, B. Tian, J. Amador-Astua, E. D. Maloney, and G. N. Kiladis, 2014: Tropical intraseasonal modes of the atmosphere. *Annu. Rev. Environ. Resour.*, **39**, 189–215, doi:10.1146/annurev-environ-020413-134219.

Sobel, A. H., and C. S. Bretherton, 1999: Development of synoptic-scale disturbances over the summertime tropical northwest Pacific. *J. Atmos. Sci.*, **56**, 3106–3127, doi:10.1175/1520-0469(1999)056<3106:DOSSDO>2.0.CO;2.

——, and E. D. Maloney, 2000: Effect of ENSO and the MJO on western North Pacific tropical cyclones. *Geophys. Res. Lett.*, **27**, 1739–1742, doi:10.1029/1999GL011043.

Stan, C., M. Khairoutdinov, C. A. DeMott, V. Krishnamurthy, D. M. Straus, D. A. Randall, J. L. Kinter, and J. Shukla, 2010: An ocean-atmosphere climate simulation with an embedded cloud resolving model. *Geophys. Res. Lett.*, **37**, L01702, doi:10.1029/2009GL040822.

Straub, K. H., and G. N. Kiladis, 2003: Interactions between the boreal summer intraseasonal oscillation and higher-frequency tropical wave activity. *Mon. Wea. Rev.*, **131**, 945–960, doi:10.1175/1520-0493(2003)131<0945:IBTBSI>2.0.CO;2.

——, P. T. Haertel, and G. N. Kiladis, 2010: An analysis of convectively coupled Kelvin waves in 20 WCRP CMIP3 global coupled climate models. *J. Climate*, **23**, 3031–3056, doi:10.1175/2009JCLI3422.1.

Suzuki, T., Y. N. Takayabu, and S. Emori, 2006: Coupling mechanisms between equatorial waves and cumulus convection in an AGCM. *Dyn. Atmos. Oceans*, **42**, 81–106, doi:10.1016/j.dynatmoce.2006.02.004.

Tai, K.-S., and Y. Ogura, 1987: An observational study of easterly waves over the eastern Pacific in the northern summer using FGGE data. *J. Atmos. Sci.*, **44**, 339–361, doi:10.1175/1520-0469(1987)044<0339:AOSOEW>2.0.CO;2.

Takayabu, Y. N., and T. Nitta, 1993: 3-5 day-period disturbances coupled with convection over the tropical Pacific Ocean. *J. Meteor. Soc. Japan*, **71**, 221–246.

Tam, C.-Y., and T. Li, 2006: The origin and dispersion characteristics of the observed tropical summertime synoptic-scale waves over the western Pacific. *Mon. Wea. Rev.*, **134**, 1630–1646, doi:10.1175/MWR3147.1.

Tulich, S., G. Kiladis, and A. Suzuki-Parker, 2011: Convectively coupled Kelvin and easterly waves in a regional climate simulation of the tropics. *Climate Dyn.*, **36**, 185–203, doi:10.1007/s00382-009-0697-2.

Waliser, D. E., and Coauthors, 2012: The ''year'' of tropical convection (May 2008–April 2010): Climate variability and weather highlights. *Bull. Amer. Meteor. Soc.*, **93**, 1189–1218, doi:10.1175/2011BAMS3095.1.

Wallace, J. M., 1971: Spectral studies of tropospheric wave disturbances in the tropical western Pacific. *Rev. Geophys.*, **9**, 557–612, doi:10.1029/RG009i003p00557.

——, and C. P. Chang, 1969: Spectrum analysis of large-scale wave disturbances in the tropical lower troposphere. *J. Atmos. Sci.*, **26**, 1010–1025, doi:10.1175/1520-0469(1969)026<1010:SAOLSW>2.0.CO;2.

Wang, B., and X. Zhou, 2008: Climate variation and prediction of rapid intensification in tropical cyclones in the western North Pacific. *Meteor. Atmos. Phys.*, **99**, 1–16, doi:10.1007/s00703-006-0238-z.

Weare, B. C., and J. S. Nasstrom, 1982: Examples of extended empirical orthogonal function analyses. *Mon. Wea. Rev.*, **110**, 481–485, doi:10.1175/1520-0493(1982)110<0481:EOEEOF>2.0.CO;2.

Wu, L., Z. Wen, T. Li, and R. Huang, 2014: ENSO-phase dependent TD and MRG wave activity in the western North Pacific. *Climate Dyn.*, **42**, 1217–1227, doi:10.1007/s00382-013-1754-4.

Wu, P., Y. Fukutomi, and J. Matsumoto, 2011: An observational study of the extremely heavy rain event in northern Vietnam during 30 October-1 November 2008. *J. Meteor. Soc. Japan*, **89A**, 331–344, doi:10.2151/jmsj.2011-A23.

Xavier, P. K., and Coauthors, 2015: Vertical structure and physical processes of the Madden-Julian oscillation: Biases and uncertainties at short range. *J. Geophys. Res. Atmos.*, **120**, 4749–4763, doi:10.1002/2014JD022718.

Xiang, B., M. Zhao, X. Jiang, S.-J. Lin, T. Li, X. Fu, and G. Vecchi, 2015: The 3–4-week MJO prediction skill in a GFDL coupled model. *J. Climate*, **28**, 5351–5364, doi:10.1175/JCLI-D-15-0102.1.

Xie, S. P., H. M. Xu, N. H. Saji, Y. Q. Wang, and W. T. Liu, 2006: Role of narrow mountains in large-scale organization of Asian monsoon convection. *J. Climate*, **19**, 3420–3429, doi:10.1175/JCLI3777.1.

Yoshida, R., and H. Ishikawa, 2013: Environmental factors contributing to tropical cyclone genesis over the western North Pacific. *Mon. Wea. Rev.*, **141**, 451–467, doi:10.1175/MWR-D-11-00309.1.

Zehr, R., 1992: Tropical cyclogenesis in the western north Pacific. NOAA Tech. Rep. NESDIS 61, 181 pp.

Zhao, H., and G. B. Raga, 2014: The influence of large-scale circulations on the extremely inactive tropical cyclone activity in 2010 over the western North Pacific. *Atmósfera*, **27**, 353–365, doi:10.1016/S0187-6236(14)70034-7.

——, P.-S. Chu, P.-C. Hsu, and H. Murakami, 2014: Exploratory analysis of extremely low tropical cyclone activity during the late-season of 2010 and 1998 over the western North Pacific and the South China Sea. *J. Adv. Model. Earth Syst.*, **6**, 1141–1153, doi:10.1002/2014MS000381.

——, X. Jiang, and L. Wu, 2015: Modulation of northwest Pacific tropical cyclone genesis by the intraseasonal variability. *J. Meteor. Soc. Japan*, **93**, 81–97, doi:10.2151/jmsj.2015-006.

Zhou, C., and T. Li, 2010: Upscale feedback of tropical synoptic variability to intraseasonal oscillations through the nonlinear rectification of the surface latent heat flux. *J. Climate*, **23**, 5738–5754, doi:10.1175/2010JCLI3468.1.

Zhou, X. Q., and B. Wang, 2007: Transition from an eastern Pacific upper-level mixed Rossby-gravity wave to a western Pacific tropical cyclone. *Geophys. Res. Lett.*, **34**, L24801, doi:10.1029/2007GL031061.